

University of Rhode Island

DigitalCommons@URI

SURFO Technical Reports

Graduate School of Oceanography

2017

SURFO Technical Report No. 17-01

SURFO

Follow this and additional works at: https://digitalcommons.uri.edu/surfo_tech_reports

Recommended Citation

SURFO, "SURFO Technical Report No. 17-01" (2017). *SURFO Technical Reports*. Paper 14.
https://digitalcommons.uri.edu/surfo_tech_reports/14

This Periodical is brought to you by the University of Rhode Island. It has been accepted for inclusion in SURFO Technical Reports by an authorized administrator of DigitalCommons@URI. For more information, please contact digitalcommons-group@uri.edu. For permission to reuse copyrighted content, contact the author directly.

**Papers from the
SUMMER UNDERGRADUATE RESEARCH FELLOWSHIP PROGRAM IN
OCEANOGRAPHY**

at

**THE UNIVERSITY OF RHODE ISLAND
GRADUATE SCHOOL OF OCEANOGRAPHY**

Narragansett, Rhode Island

June – August 2017



This program was supported by The National Science Foundation
REU Program (OCE-1460819)

GSO Technical Report No. 17-01

TABLE OF CONTENTS

Table of Contents	iii
Participants in the 2017 Fellowship Program	v
Site Directors' Preface	vi
Nutrients and nitrogen fixation across the Gulf Stream <i>Elana Ames and Jamie Palter</i>	1
<i>Pseudo-nitzschia</i> in Narragansett Bay: Identification based on morphology and growth response to irradiance <i>Rosalie Cissé, Lucie Maranda and Jan Rines</i>	4
Hurricane landfall <i>Salvatore Ferrone and Isaac Ginis</i>	11
Exploring the relationship between genetic variance in ComEC and uptake efficiency in natural transformation <i>Madison Flasco and Ying Zhang</i>	23
Overcoming barriers to motivate community action to enhance resilience <i>Courtney Hill, Donald Robadue and Pamela Rubinoff</i>	26
Multi-environmental growth assessment plate: A new method of conducting temperature dependent growth experiments with phytoplankton <i>Kierra Jones, Stephanie Anderson and Tatiana Ryneason</i>	29
Nutrient cycling of the Southern Ocean during late summer <i>Amanda Love and Rebecca S. Robinson</i>	35
Submerged Paleo-Shorelines as Markers of Vertical Deformation around Lake Azuei, Haiti <i>Oliver Lucier and Marie-Hélène Cormier</i>	43
Spectral characteristics of a variety of open ocean regions <i>Nicholas Piskurich, Baylor Fox-Kemper and Peter Cornillon</i>	54
Interactions of euphausiid distributions in the Eastern Tropical North Pacific with the oxygen minimum zone <i>Shannon Riley and Karen Wishner</i>	64
A low-cost Lagrangian float prototype for observations of the biological carbon pump <i>Jackson Sugar and Melissa Omand</i>	78
Optics and phytoplankton in Narragansett Bay, RI <i>Kyle Turner and Colleen Mouw</i>	86

2017 PROGRAM PARTICIPANTS
SUMMER UNDERGRADUATE RESEARCH FELLOWSHIP IN OCEANOGRAPHY

FELLOWS

Elana Ames, Coastal Carolina University (Marine Sciences)
Rosalie Cissé, Tougaloo College (Biology)
Salvatore Ferrone, Ithaca College (Physics)
Madison Flasco, Otterbein University (Mathematics, Biology)
Courtney Hill*, Tougaloo College (Psychology, Biology)
Kierra Jones, Tougaloo College (Biology)
Amanda Love, Lake Superior State University (Chemistry)
Oliver Lucier, Rice University (Earth Sciences)
Nicholas Piskurich, Notre Dame University (Environmental Engineering,
Shannon Riley, Oregon State University (Ocean Science, Marine Biology)
Jackson Sugar, University of Rhode Island (Ocean Engineering)
Kyle Turner, George Mason University (Earth Science)
Melanie Wallace, Purdue University (Multidisciplinary Engineering)

*participating with other-than-SURFO funding

ADVISORS

Marie-Hélène Cormier
Peter Cornillon
Isaac Ginis
Lucie Maranda
Colleen Mouw
Melissa Omand
Jaime Palter
Jan Rines
Donald Robadue
Rebecca Robinson
Pamela Rubinoff
Tatiana Rynearson
Matt Wei
Karen Wishner
Ying Zhang

PROGRAM ASSISTANTS

Christine Gardiner, URI Student Liaison
Kim Carey, Program Coordinator

PREFACE

This report presents the papers written by the 13 participants in the ten weeks of the 2017 Summer Undergraduate Research Fellowships in Oceanography (SURFO) program at the Graduate School of Oceanography (GSO), University of Rhode Island (URI). The papers are introduced in alphabetical order of the participants. Ten papers follow manuscript-style presentation, whereas three are written to satisfy the proposal requirements for application to the National Science Foundation Graduate Research Fellowship Program. This 2017 summer represented the 33rd consecutive year in which the program has been coordinated and extended through the several disciplines in oceanography and ocean engineering at URI's Narragansett Bay Campus. The activities continue excellence beyond the official duration of the program with presentations at national conferences: four projects for a total of six presentations accepted for the 2018 Ocean Sciences Meeting in Portland (OR), and two presentations from one project for the AGU 2017 Fall Meeting in New Orleans (LA). SURFOs are first authors on three posters and one oral presentation, and co-authors on all the others. One manuscript (Wei and Wallace) is in preparation. Others will be part of publications in the near future.

Co-director Donohue will present a poster at the 2018 Ocean Sciences Meeting on the retrospective assessment of the program over its 33-year duration.

The 2017 SURFO participants are grateful to the National Science Foundation REU program for their support through grant OCE-1460819. The SURFO program sincerely thanks advisors and graduate student mentors at URI who contributed to the program's success including those who gave SURFO seminar presentations and/or participated in various educational activities. In addition, our thanks go to Kim Carey for her timely assistance covering administrative, financial, and initial recruitment tasks. Finally, we acknowledge Christine Gardiner who served as the program student liaison.

Lucie Maranda
Kathleen A. Donohue
David C. Smith
SURFO Site Directors

December 2017

NUTRIENTS AND NITROGEN FIXATION ACROSS THE GULF STREAM

Elana Ames¹ and Jamie Palter²

¹Department of Marine Science, Coastal Carolina University, Myrtle Beach, SC

²Graduate School of Oceanography, University of Rhode Island, Narragansett, RI

Abstract

Primary productivity in the ocean's subtropical gyres is limited by nutrient deficiencies. When nitrogen is scarce and phosphate and iron are available, microorganisms known as diazotrophs can fix elemental nitrogen gas into its bio-available form. This is an energetically costly process and therefore diazotrophs are thought to be out-competed when bio-available nitrogen is abundant. It is also often assumed that diazotrophs can only be found in warm, well-stratified waters; this assumption has not been vigorously tested. In the subtropical North Atlantic, excess phosphate is transported across the Gulf Stream by wind and eddy driven mechanisms, and may support nitrogen fixing organisms in the region just south of the jet. To investigate the flux of nutrients and nitrogen fixation across the Gulf Stream and in the subtropical gyre, data were collected from the top 1000 m of the water column along a transect across the jet during 25-30 April 2017. These data were analyzed for velocity, temperature, oxygen, salinity and nutrients. Nutrient content and physical characteristics agree with previous studies and in accordance with the Ekman transport, indicate a source of P* from outside of the subtropical gyre, north of the Gulf Stream. Historical data also show that at least one type of diazotroph is present in the region of interest. Various other methods are in process to quantify the nitrogen fixation rates in the water column and implement molecular analysis on the *nifH* gene abundance. These pending outcomes will help determine if and how much N₂ fixation is taking place.

Proposal to the National Science Foundation Graduate Research Fellowship Program

Iron transport across the Gulf Stream

(The rest of this section intentionally left blank)

***Pseudo-nitzschia* in Narragansett Bay: Identification Based on Morphology and Growth Response to Irradiance**

Rosalie Cisse¹, Lucie Maranda², and Jan Rines²

¹ Department of Biology, Tougaloo College, Tougaloo, Mississippi

² Graduate School of Oceanography, University of Rhode Island, Narragansett, Rhode Island
Corresponding author: Rosalie Cisse (rose.cisse153@gmail.com)

Running head: Morphology and growth of *Pseudo-nitzschia*

Key Points:

- Some *Pseudo-nitzschia* may develop into toxic blooms that have extensive effects on humans and economy
- Light and scanning electron microscopy are two ways to identify species of *Pseudo-nitzschia*
- *Pseudo-nitzschia* can grow in low light levels

Key Index Words:

diatoms, *Pseudo-nitzschia*, domoic acid, *Ditylum brightwellii*

Abstract

Diatoms are microscopic, eukaryotic phytoplankton that carry out 20 percent of Earth's photosynthesis. Only one genus of diatom, *Pseudo-nitzschia* (PN), is known to contain toxic species that can cause harmful algal blooms. In the fall of 2016 and the winter of 2017 in Narragansett Bay, there were two *Pseudo-nitzschia* blooms that tested positive for domoic acid. This particular acid can accumulate in shellfish in the water; humans would later eat these shellfish and experience stomach pain, neurotoxic symptoms, specifically amnesia, and in rare cases death. One of the main objectives of this project was to gain insight on which species of *Pseudo-nitzschia* were present in the blooms of Narragansett Bay and to further understand its morphology by using light (LM) and scanning electron microscopy (SEM). Previous research has suggested that this genus may have an unusual ability to persist at low light levels. Therefore, our second objective was to experimentally determine the level of light that limits growth in *Pseudo-nitzschia*. There were favorable results from the light experiment. There was a constant growth in the culture of *Pseudo-nitzschia* as well as the *Ditylum* that was inoculated to compare to the PN. The clonal culture of PN was successfully identified at *P. pungens*.

1. Introduction

Diatoms are microscopic, eukaryotic phytoplankton that make up 20% of the Earth's photosynthesis (Armbrust 2009). They can be identified as centric, with a radial symmetry, or as pennate, with a bilateral symmetry. All diatoms have a cell wall made of silica. The pennate genus *Pseudo-nitzschia* is commonly found in coastal waters. Some species of PN contain domoic acid, a toxic acid. When present, domoic acid causes Amnesic Shellfish Poisoning (ASP). The first record of domoic acid in phytoplankton was in 1987 in Canada (Trainer 2011). Domoic acid does not only affect ocean life, but also human life and economy. Humans become poisoned when consuming shellfish with toxic PN. The negative economic effects include the closing of

shellfish harvest, whether cultured or wild, as tainted shellfish cannot be sold. Narragansett Bay experienced its first toxic blooms of PN with domoic acid in the fall of 2016 and the winter of 2017. There were many hypotheses as to where the blooms could have originated from. The blooms were hypothesized to have originated from currents bringing the PN from offshore waters into the Bay or there could have been changes in the toxicity of a local bloom. Other hypotheses suggest that the blooms were present in the past but their toxicity was not detected; there also could have been a hidden inoculum population.

Literature suggests that some species of PN can thrive at low levels of light (Rines 2008). We conducted a light limitation experiments to test this theory. Cultures of *Ditylum* were used for comparison. The purpose was to be able to refute whether light levels only seriously affected PN or other diatoms as well.

There are 6 known species of PN in the bay (Hargraves and Maranda 2002). Light and scanning electron microscopy was used toward the identification of one PN clone.

2. Materials and Methods

Surface water was collected from GSO pier on Narragansett Bay in June 2017 and was concentrated using a 20- μm filter. *Pseudo-nitzschia* clone B6 and *Ditylum brightwellii* clone M49-17-1B were successfully isolated for subsequent use in light limitation experiments. Both diatom clones were maintained in f/2 medium (Guillard and Ryther 1962) at 15°C on a 12:12 L:D cycle. Experiments were conducted in triplicate Erlenmeyer flasks containing 125 mL of medium. Three light levels were created using neutral density screening. Light levels were measured with a Biosphericals Instruments QSL 2101 PAR light meter (Table 1).

Table 1. Average light levels to which the triplicate flasks were exposed.

	Average Light Levels ($\mu\text{mol photons/m}^2/\text{s}$)
Full Light	256
L1	89
L2	33

To initiate the experiments, 100 μL of Lugol's Iodine solution was added to 10 mL of a stock culture in order to halt the motility of *Pseudo-nitzschia* colonies so that they could be enumerated in a Sedgwick-Rafter chamber. An inoculum was then calculated to result in initial experimental concentrations of 70 cells mL^{-1} for *Pseudo-nitzschia* and 30 cells mL^{-1} for *Ditylum*. Each taxon was studied in sequential experiments. Growth rate (k) was calculated using this formula:

$$k = (\ln(N_1/N_0) / (t_1 - t_0)) / \ln 2$$

where N_1 and N_0 are cell density in Relative Fluorescence units (RFU) measured, and t_1 and t_0 are time (hours) (Stein 1973). Cell density was measured in 24-well microtiter plates every day for five days on a Spectramax M5 plate reader.

Pseudo-nitzschia clone B6 was identified using light microscopy. We measured the length, width, and amount of overlap between cells. Scanning electron microscope was used to help determine the number of ribs in 10 micrometers and to count the number of pores between ribs. Under the light microscope, live material could be identified. To oxidize the sample, hydrogen peroxide (30%) was used. The sample also needed to be desalinated. This clean material was then used to make permanent slides for high resolution light microscopy and mount for the scanning electron microscope. A key from Hasle and Syversten (1996) was used to identify the species of *Pseudo-nitzschia*.

3. Results

Pseudo-nitzschia showed a range of growth between 1.12 and 2.47 divisions/day, with the smallest amount of growth in L2 (Table 2).

Table 2. Growth rates (divisions/day) for *Pseudo-nitzschia* and *Ditylum* as a function of irradiance. Measurements of PN on one L2 sample were stopped being tested after two days because of spillage. Measurements of *Ditylum* in L1 yielded only two growth rate data points.

Species	FL	L1	L2
<i>Pseudo-nitzschia</i>	1.15	1.9	1.12
	2.32	1.82	1.27
	1.88	2.47	
<i>Ditylum</i>	1.66	1.42	1.03
	1.82	1.43	0.9
	1.75		1.21

Divisions/day for *Pseudo-nitzschia* and *Ditylum* show that there was a difference in growth rate due to irradiance. Both species growth rates are also influenced by irradiance, so there was a significant difference (0.014) in the response of the cells in relation to Light (Table 3).

Table 3. Analysis of variance summary table for species and irradiance effects. A probability of less than 0.05 is considered significant.

Factor	Df	Sum Sq	Mean Sq	F value	Pr(>F)
Species	1	0.4590	0.4590	4.490	0.06
Irradiance	2	1.3834	0.6917	6.766	0.014*
Species: irradiance	2	0.2593	0.1297	1.268	0.32
Residuals	10	1.0224	0.1022		

Table 4 Analysis of variance with factor irradiance, with species analyzed separately.

	Df	Sum Sq	Mean Sq	F value	Pr(>F)
<i>Pseudo-nitzschia</i>	2	0.9133	0.4567	2.376	0.19
Residuals	5	0.9610	0.1922		
<i>Ditylum</i>	2	0.7294	0.3647	29.7	0.0017 **
Residuals	5	0.0614	0.0123		

The constant growth of *Ditylum* and *Pseudo-nitzschia* in both graphs show that diatoms are able to grow in lower levels of light (Figures 1 and 2). Cultures under FL and L1 did not show significant differences in irradiance, but cultures in L1 had much more irradiance than L2. After some initial mortality, *Pseudo-nitzschia* displayed similar growth rate, regardless of the light level.

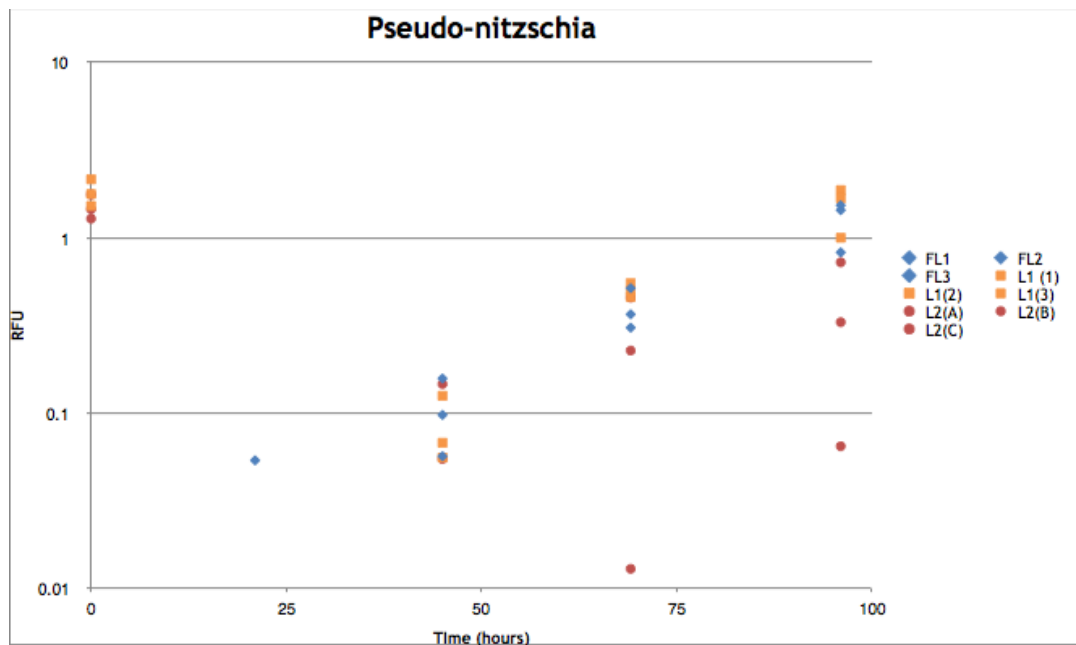


Figure 1: Growth of *Pseudo-nitzschia* measured as relative fluorescence unit (RFU) as a function of time in hours. The different colors indicate the different light levels the triplicates were subjected to. Blue: full light, orange: one screening, red: two screenings (minimal light).

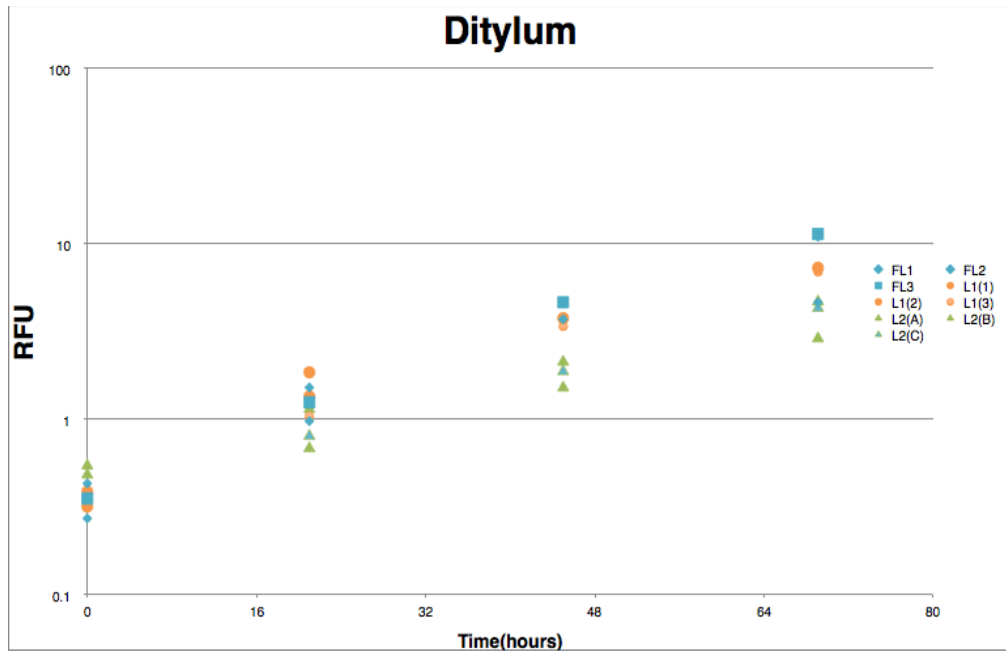


Figure 2: Growth of *Ditylum* measured in relative fluorescence unit (RFU) as a function of time (hours). Contrary to Figure 1, *Ditylum* did not experience any initial mortality. *Ditylum* showed a range of growth between 0.9 to 1.8, with the smallest amount of growth in L2. Although growth rates were very close, they were significantly different. The light levels are the same as the one from Figure 1.

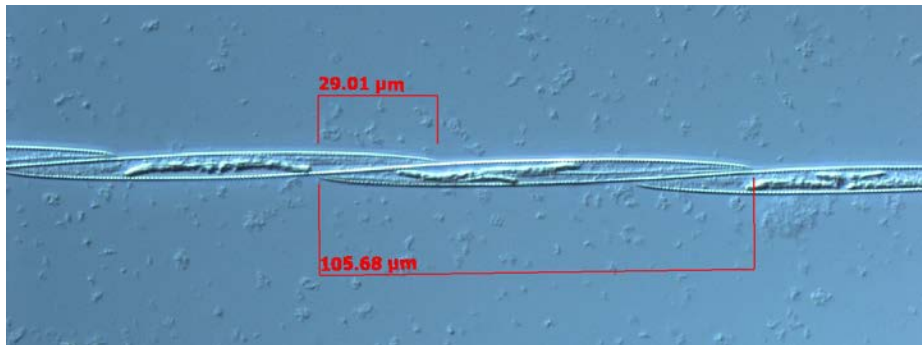


Figure 3: Chain of *Pseudo-nitzschia*

Based on light microscope observations of both living and cleaned material, *Pseudo-nitzschia* clone B6 was identified using the key in Hasle & Syvertsen (1996). Morphological data included the length of the apical and transapical axes, the amount of overlap of adjacent cells in a colony, symmetry with respect to the apical axis, presence/absence of a central interspace, and characteristics of the fibulae, virgae and areolae.

The apical axis measured 104-106 μm , the transapical axis 4.3 μm , fibulae were visible in the light microscope, and two rows of poroids could barely be discerned under 100x oil immersion

phase contrast optics (Figures 3, 4, and 5). Overlap of adjacent cells was approximately one quarter of the apical axis. The presence of these features suggests that clone B6 is most likely *Pseudo-nitzschia pungens*. This taxon is generally not known to produce domoic acid, thus is probably not responsible for the toxic events in Narragansett Bay.

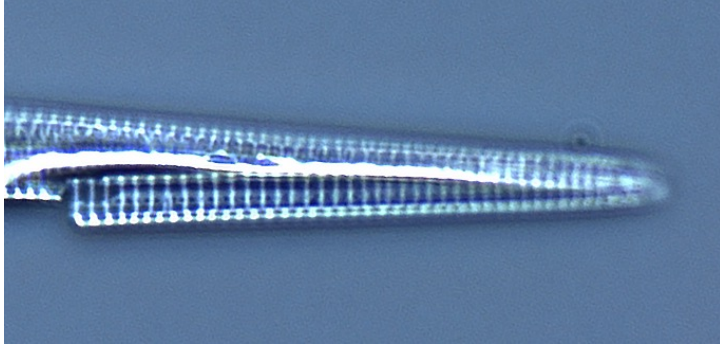


Figure 4: 100x oil immersion image of the pores in a cleaned PN valve

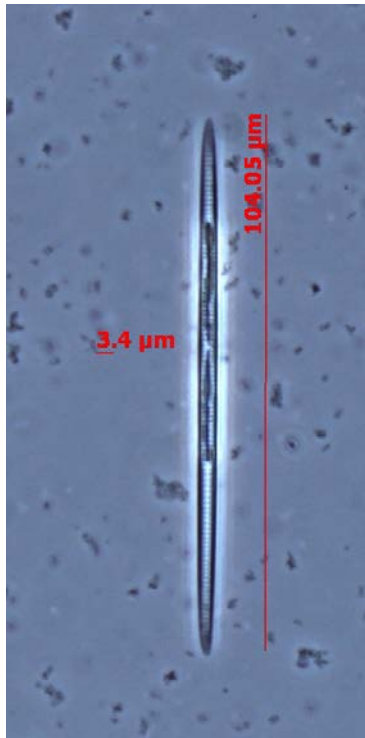


Figure 5: Single cell of *Pseudo-nitzschia* in valve view showing apical and transapical measurements, phase contrast.

4. Discussion

Because the factor species was so close to .05, growth rate data for the two species were analyzed separately and yielded a significant difference in growth rate in irradiance for *Ditylum* but not for *Pseudo-nitzschia*.

We were not able to gather data that would have further confirmed the species of *Pseudo-nitzschia* that was in the clonal culture of B6. This experiment should be conducted numerous

times for more analytical data. Early preparation of the scanning electron microscope would also be suggested so that data could be obtained from it.

5. Conclusions

The focal point of this paper stems from diatom toxic blooms in Narragansett Bay. Toxic blooms in the bay do not only affect aquaculture but also the humans that are part of the intricate food web of the ocean. Domoic acid in *Pseudo-nitzschia* might be new to the bay but it has been recorded all over the world. The purpose of this paper was to evaluate whether or not it was possible for PN to grow in lower light levels than was usually expected. The data were able to confirm that PN as well as *Ditylum* were able to grow in lower light levels. The other focal point of this paper was the morphology of the clonal culture of PN. Using the key from Hasley and Silversten 1996, the morphology of the clonal culture B6 was quickly identified as *Pseudo-nitzschia pungens*. This species of PN is generally harmless in the bay. In the future, knowing which species of PN are in the bay would help better manage the problem quickly as well as fence any panic from the general population.

Acknowledgment

RC was supported by a Summer Undergraduate Research Fellowship in Oceanography (SURFO) (National Science Foundation REU grant # OCE-1460819). I would also like to profusely thank Dr. Lucie Maranda and Dr. Jan Rines for giving me an opportunity to work with them in their labs and for them being tremendously patient with me as I attempted to learn all that I could about marine science.

References

- Armburst, E. Virginia. "The Life of Diatoms in the World's Oceans ." *Nature*, vol. 459, 14 May 2009, p. 185
- Guillard, R. R. L. and J. H. Ryther 1962. Studies of marine planktonic diatoms. I. *Cyclotella nana* Hustedt and *Detonula confervacea* (Cleve) Gran. *Can. J. Microbiol.* 8: 229-239.
- Hargraves, P. E. and L. Maranda 2002. Potentially toxic or harmful microalgae from the northeast coast. *The Northeastern Naturalist* 9 (1): 81-120.
- Rines, Jan E.B. "Thin Layers and Species-Specific Characterization of the Phytoplankton Community in Monterey Bay, California, USA." *Continental Shelf Research*, vol. 30, 15 Jan. 2010, pp. 67-79.
- J.R. Stein, Phycological Society of America INC. 1973. *Division Rates*. Vancouver, Canada: Cambridge University Press
- Trainer, Vera L. "*Pseudo-nitzschia* Physiological Ecology, Phylogeny, Toxicity, Monitoring and Impacts on Ecosystem Health ." *Harmful Algae*, pp. 271-273.

Evaluating the Performance of WAVEWATCH III under Hurricane Forcing Winds in Shallow Water

Salvatore Ferrone¹, Isaac Ginis², and Xuanyu Chen²

¹Department of Physics and Astronomy, Ithaca College, Ithaca, New York

²Graduate School of Oceanography, University of Rhode Island, Narragansett, Rhode Island

Corresponding author: Salvatore Ferrone (sferrone@ithaca.edu)

Running head: Performance of WAVEWATCH III

Key Points:

- WAVEWATCH III, an ocean surface wave model evaluated under landfalling hurricane conditions
- WAVEWATCH III accurately assesses spatial variability of significant wave height
- WAVEWATCH III generally overestimates the significant wave height in very high wind conditions

Key Index Words:

WAVEWATCH III, Hurricane Bonnie, Scanning Radar Altimeter, National Data Buoy Center

Abstract

The goal of this project is to evaluate the performance of the computer modeling program for ocean surface wave, WAVEWATCH III, under land falling hurricane conditions. WAVEWATCH III is used for ocean wave characteristic predictions maintained by the Environmental Modeling Center (EMC) under the National Oceanic and Atmospheric Administration (NOAA). These characteristics include dominant wavelength, significant wave height, and wave direction. Previous versions of WAVEWATCH III accurately predicted hurricane waves over open-ocean depths deeper than 30 m, yet lost accuracy when hurricanes enter regions of shallow water, 30 m or less. More aspects of shallow water ocean physics such as bottom friction, depth-induced wave breaking, and wave refraction are included in the new WAVEWATCH III v5.16. To determine if the new model improves the performance in shallow water regions, we simulate ocean waves under Hurricane Bonnie (1998) and compare the results to NASA's Scanning Radar Altimeter (SRA) and the National Data Buoy Center's (NDBC) observational data. We have determined that WAVEWATCH III v5.16 accurately predicts the spatial variability of the significant wave height, yet generally overestimates the significant wave height.

1. Introduction

WAVEWATCH III (WW3) is a computer modeling system for predicting ocean surface waves. This study evaluates WW3's performance for predicting ocean surface waves using observational data during Hurricane Bonnie. A similar study had been done previously by Moon et al (2003). However, since that time the WW3 has been updated to include more aspects of shallow water physics such as depth induced wave breaking, bottom friction and wave refraction.

We are particularly interested in the model predictions of ocean surface waves in shallow water with ocean depths less than 30 m with the aim to improve storm surge predictions. We compared WW3 predictions of the significant wave height for Hurricane Bonnie on August 26, 1998 to observations made by the National Aeronautics and Space Administration's Scanning Radar Altimeter (SRA) and the National Data Buoy Center's (NDBC). We also compared the model predictions in the open ocean against data provided by the SRA and compared our model results with previous work done by Moon et al (2003).

Modeling ocean surface waves helps to alleviate the limitation associated with the nearly impossible task of making wave observations spanning large ocean distances. Despite computer models being our best method of predicting the ocean surface waves, there are some shortcomings associated with the modeling. These include numerical approximations of the governing equations, incomplete physics, and uncertainties associated with input parameters. This study focuses on the evaluation and verification of WW3's newest version that became operational at NOAA's National Weather Service under land falling hurricane conditions in shallow waters. A skillful wave model is important for predicting possible hazardous conditions for ship navigators in coastal and open ocean regions and storm surges during hurricane landfall.

1.1 The WAVEWATCH III Model

Modeling ocean surface waves began in 1944 when the allies planned to invade the beaches of Normandy. Since then, various wave models have been used operationally to predict ocean surface waves. Some of the shortcomings of previous models were the inability to accurately predict waves for complex, fast varying wind fields, i.e. in hurricane conditions (Tolman 2002). WW3 was developed by NOAA to overcome these issues as well as develop a flexible computer program that can be easily adjusted for new updates in physics. The model became operational in March of 2000.

Being a widely used third-generation wave model, WW3 predicts ocean surface waves by solving the wave action equation (Fan et al. 2009). WW3 is called a "third-generation" wave model, which means that it explicitly solves the full nonlinear equations predicting the directional wavenumber (or frequency) spectrum and its evolution as waves propagate. The directional wavenumber spectrum is used for calculating output wave parameters such as the significant wave height, mean wavelength, etc. For this study, the wave model is set up as follows. The frequency space is discretized into 40 bins, ranging from 0.0285 to 1.1726 Hz with a logarithmic increment factor of 1.1; the direction space is discretized into 24 bins. These are the same settings used in Fan et al (2009). The wind input and whitecapping source terms used in this simulation are from Tolman and Chalikov (ST2), which was used in the previous operational hurricane wave forecast. Standard discrete interaction approximation (DIA) is used for computing the nonlinear interaction term. Since version 4.18, shallow water physics have been introduced into WW3. For this study, JONSWAP parameterization is used to compute dissipation due to the bottom friction; Battjes and Janssen parameterization is used to compute depth-induced breaking; and triad interaction is activated. All tuning parameters in the above physic packages are set as default.

In short, WAVEWATCH III operates by inputting a wind field and outputting the ocean surface waves. The wind field consists of wind vectors with a specified spatial and temporal resolution.

For example, wind vectors spaced every one twelfth degree of latitude and longitude, and sampled every 15 minutes in time.

1.2 Hurricane Bonnie

Hurricane Bonnie occurred from the 22nd of August 1998 and dissipated on August 29 1998 (Figure 1). It was a major (Category 3 on the Saffir-Simpson Hurricane Scale) hurricane during landfall in North Carolina on August 27. The storm had maximum reported wind speed of 115 miles per hour and a minimum pressure of 954 millibars. In the United States, Bonnie caused an estimated \$1 billion in damage; two people drown in rip currents.

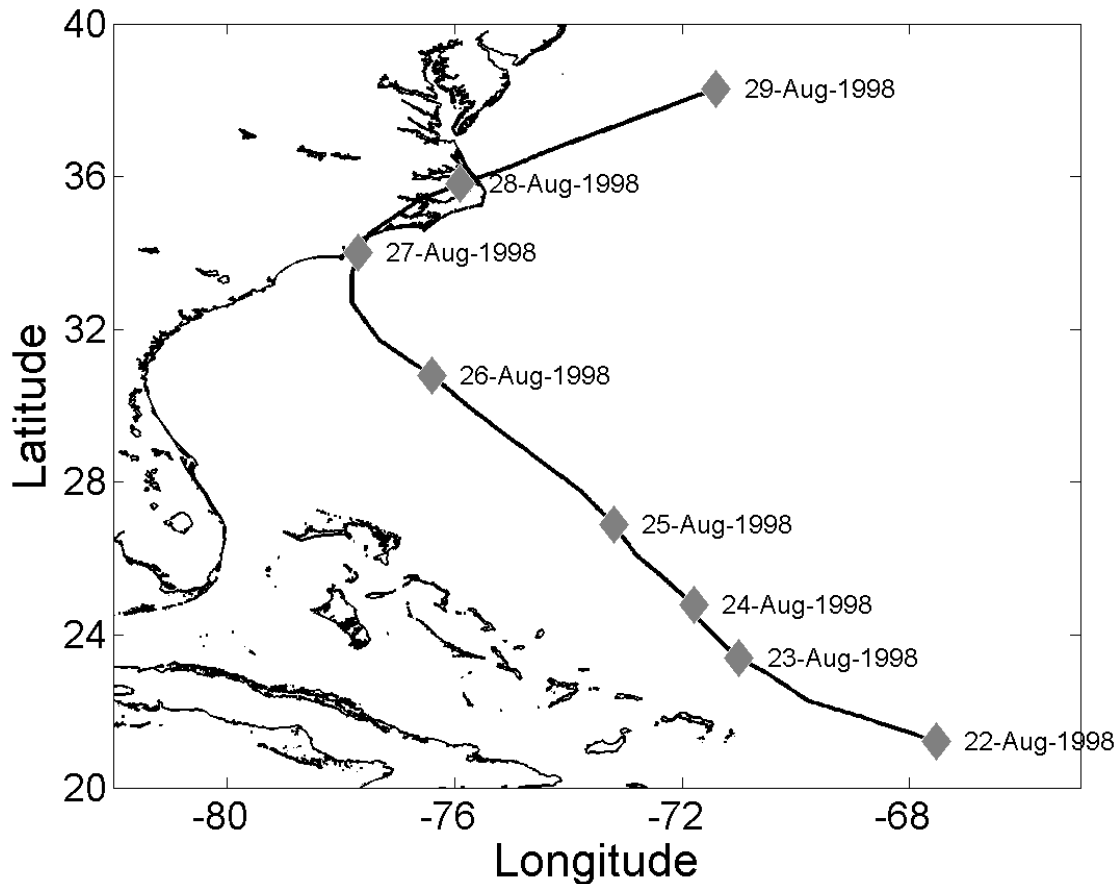


Figure 1. The path of Hurricane Bonnie in August 1998. The x and y-axis represent the longitude and latitude of the Earth respectively. The east coast of the United States, the Bahamas, and Cuba are shown by the black lines in the left side of the figure. The thick black line represents the path of Hurricane Bonnie. The diamond markers show the position of Bonnie at midnight on the dates specified in the figure.

2. Materials and Methods

The general flow of this study is: create a hurricane wind field from the storm parameters provided by the National Hurricane Center, verify that the wind field is consistent with buoy observations, use the wind as input to run WW3, and compare WW3's ocean surface wave

results to the National Aeronautical and Space Administration's Scanning Radar Altimeter observations.

2.1 The Wind Field

The hurricane wind fields for Bonnie is generated based on methods used in Moon et al. (2003), with the best-track data provided by the National Hurricane Center every six hours (<http://www.nhc.noaa.gov/data/>). The parameterization constructs a radial wind profiles based on several key parameters: the maximum winds, the radius of maximum winds, 4-quadrant radius of 34-knot and 50-knot winds, the ambient pressure outside of the hurricane, and the central pressure of the hurricane. If the 4-quadrant radius of 34-knot and 50-knot winds information is missing, the wind field is then created by using the Holland radial profile model (Holland 1980). After the wind profile is created, an empirical inflow angle formulation is used to create the radial (inflow) component of the hurricane winds. Also, the translation speed of the storm is added to the wind field to account for the asymmetry of the storm.

We used an additional source of observational data, H*WIND, to adjust our parametric wind field. H*WIND is a product provided by NOAA's Hurricane Research Division (HRD) (http://www.aoml.noaa.gov/hrd/data_sub/wind.html). HRD scientists use airplanes that fly into the storms and make observations of the pressure, wind speed and direction. During Hurricane Bonnie, there were only limited (6 snapshots) H*WIND data available. We used the H*WIND data in two instances, one in the open ocean and the other one at landfall to improve the parametric winds. Although not perfect, the differences between parametric winds and H*WIND are generally less than 4 m/s within 200 km from the storm center.

We verified that the wind field created is reasonable by comparing the wind speeds and directions to observations reported by the National Buoy Data Center Buoys. Figure 2 shows the location of the buoys and Figure 3 shows the comparison of the parametric wind fields versus the observational data. There is general agreement between the calculated winds and the observations. August 22nd to roughly August 25th of each graph shows larger disagreement between the parametric and observed winds. This is likely due to the fact that the parametric model does not account for environmental winds.

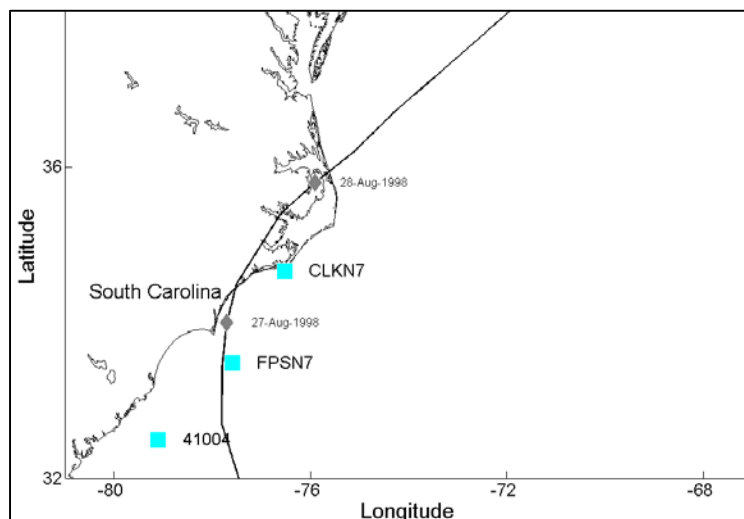


Figure 2. The path of Hurricane Bonnie in August 1998. The x and y-axis represent the longitude and latitude of the Earth respectively. The east coast of the United States, the Bahamas, and Cuba are shown by the black lines in the left side of the figure. The thick black line represents the path of Hurricane Bonnie. The diamond markers show the position of Bonnie at midnight on the dates specified in the figure. The cyan markers represent buoys used in this study.

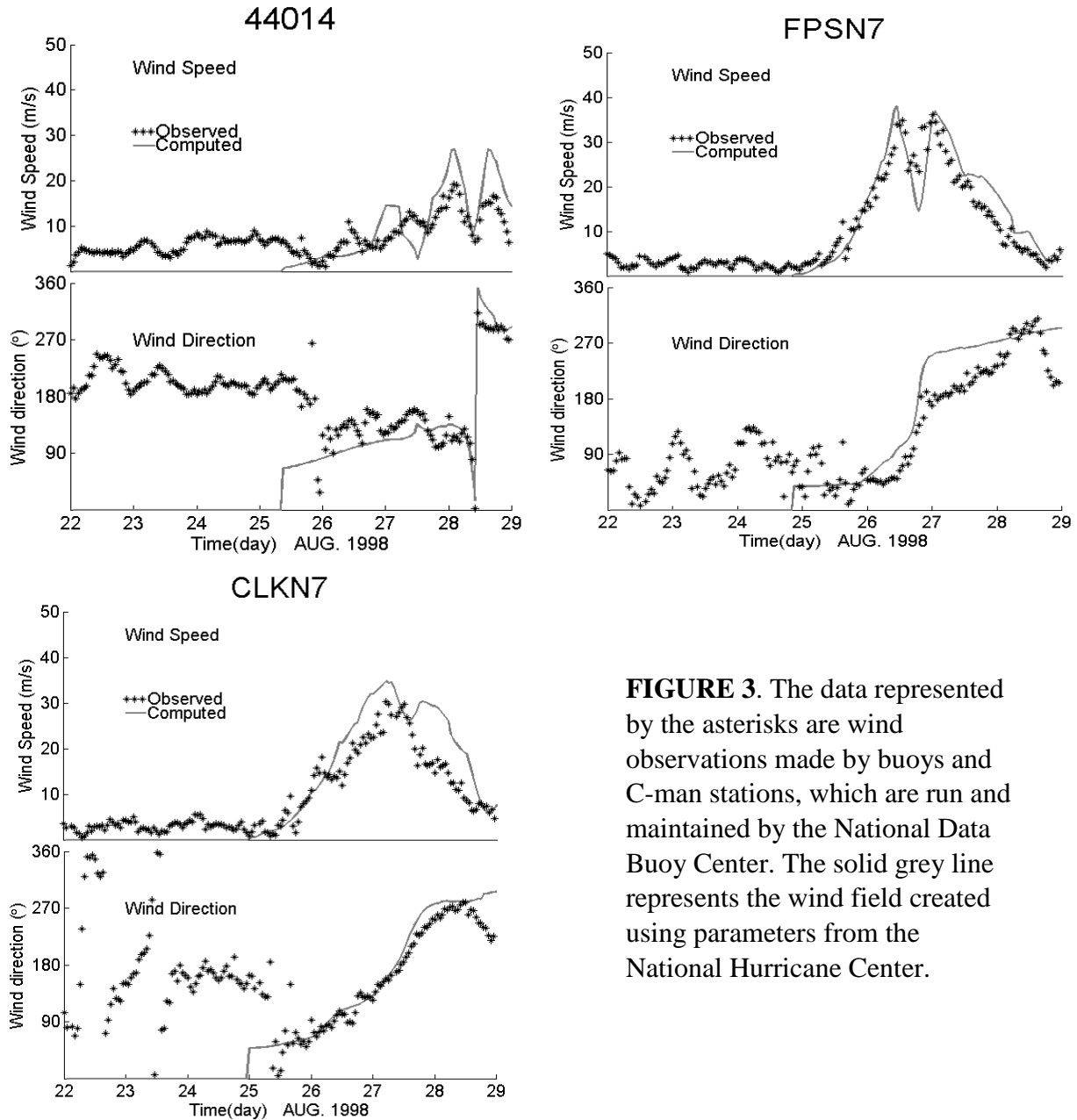


FIGURE 3. The data represented by the asterisks are wind observations made by buoys and C-man stations, which are run and maintained by the National Data Buoy Center. The solid grey line represents the wind field created using parameters from the National Hurricane Center.

2.2 National Data Buoy Center

The National Data Buoy Center operates buoys located all around the world’s oceans. These buoys make observations of the oceanic and atmospheric parameters at their locations. Three buoys shown in Figure 2 are used to verify our calculated significant wave height, wind directions, wind speed, and atmospheric pressure.

2.3 The Scanning Radar Altimeter

The Scanning Radar Altimeter (SRA) is an instrument created by NASA that scans the ocean surface to create a sea surface topographic map (Figure 4). The SRA is installed on a NOAA aircraft. On August 24 the plane penetrated the eye five times, staying airborne for over five hours (Figure 5). On August 26 the plane was in the air for another 5 hours and made measurements of the ocean surface during Bonnie's landfall (Figure 6).

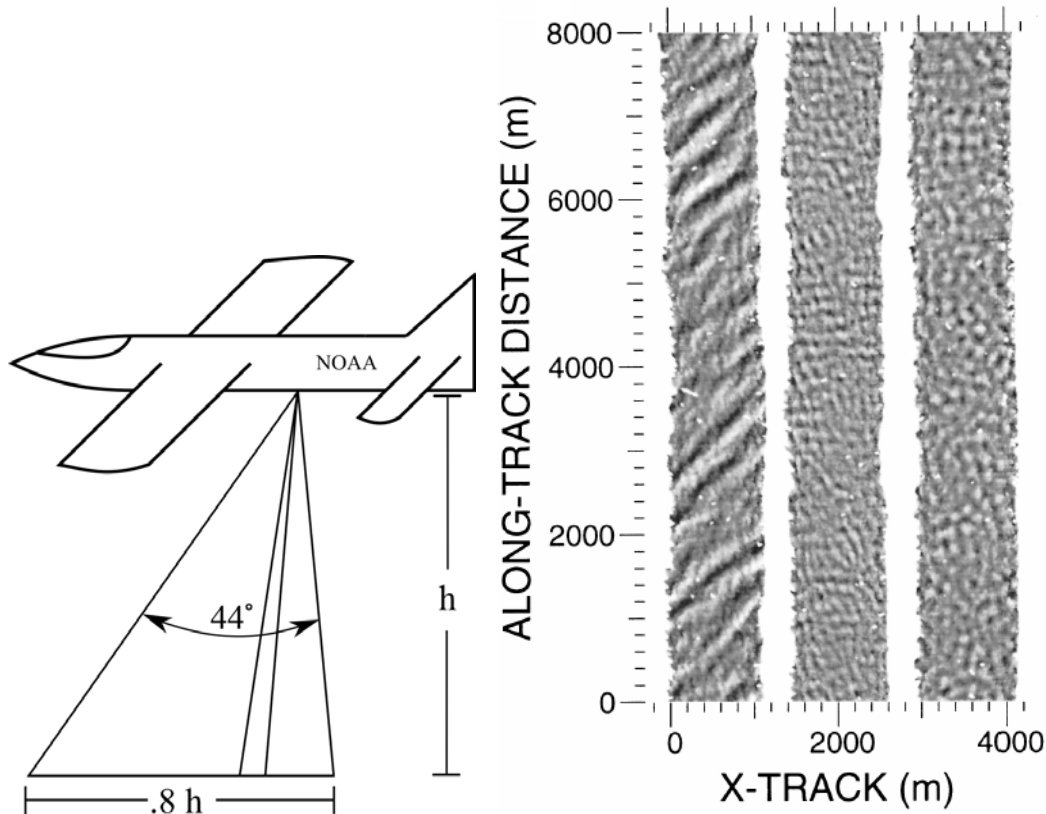


Figure 4. Geometry of the SRA installed on a NOAA aircraft (left figure) (Wright et al. 2001). The SRA uses radar to scan the track of the ocean in a side sweeping manner that is perpendicular to the trajectory of the aircraft. The ocean surface is sampled 64 times, providing a horizontal cross section which is transformed using a Fast Fourier Transform to produce sea surface topography maps (right figure). The X-TRACK represents the cross sectional distance the SRA samples. For Hurricane Bonnie the SRA flew 1500 m above sea level.

3. Results

The goal of the project is to validate WW3 predictions of ocean surface waves for land falling hurricane conditions. We compared the significant wave height modeled in the open ocean with SRA data as done in Moon et al. (2003). The waves that form over Open Ocean eventually propagate to the shore. We wanted to make sure the model open ocean waves are consistent with observations even though they are not the main focus of the study.

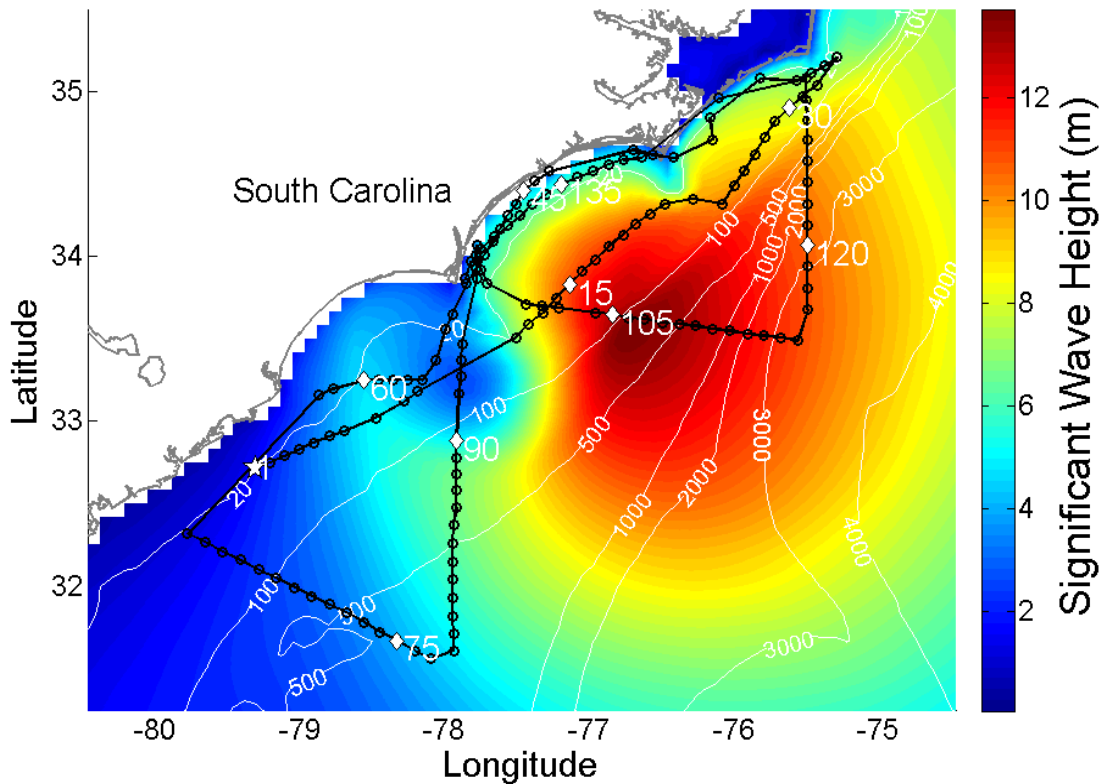


Figure 5. Path of the SRA when hurricane Bonnie made land fall on August 26 1998. The circles represent data points collected by the SRA. The white star is the first data point collected by the SRA, each white diamond is spread 15 data points apart from one another and are numbered. The color map represents the significant wave height predictions from the WW3 at 19:00 August 26th universal time. The white contour lines represent ocean bathymetry in meters.

3.1 Open Ocean

Figure 6 shows the significant wave height as predicted by WW3 for the wave field at 22:30 universal time. This is the median time of the flight taken by the hurricane hunter on August 24. The light blue circle is not the center of the eye, it is the bottom left quadrant of the storm where the waves are the smallest. The highest waves are in the front right section of the storm. In a moving hurricane shorter and smaller waves are in the rear left quadrant of the storm, and taller and longer waves in the right-front quadrant, as a result of both the asymmetric winds and the resonance effect. This expected pattern is consistent with the wave field predicted by WW3.

The WW3-SRA comparison (Figure 7) shows overall a reasonable agreement with the model over predicting the wave height at larger distances from the center and underestimating the wave height near the center of the storm.

3.2 Landfall

Observations on wave height from the path of the SRA when hurricane Bonnie made land fall (Figure 6) are compared to the significant wave height predicted by WW3 at the SRA locations (Figure 8). The comparison at the SRA locations was used instead of the distance from the center of the storm in Figure 7 for the open ocean case due to the complexity of the aircraft's flight path. This method of comparing data was used for SRA model comparison in Hurricane Ivan in Fan et al. (2009).

The significant wave height predicted by WW3 is produced as a two-dimensional wave field in latitude longitude space, at a 1/12-degree resolution. The latitude and longitude coordinates of the SRA locations were used to interpolate the WW3 simulated significant wave height at the same location.

The correlation plots in Figures 9 and 10 show WW3 predictions of the significant wave height against the SRA observations. If the data were to collapse on the dotted line (slope of 1), WW3 would predict exactly what the SRA observed. The line of best fit in Figure 9 has a slope of 1.4. Since this is greater than 1, WW3 overestimated taller waves more than it did shorter waves.

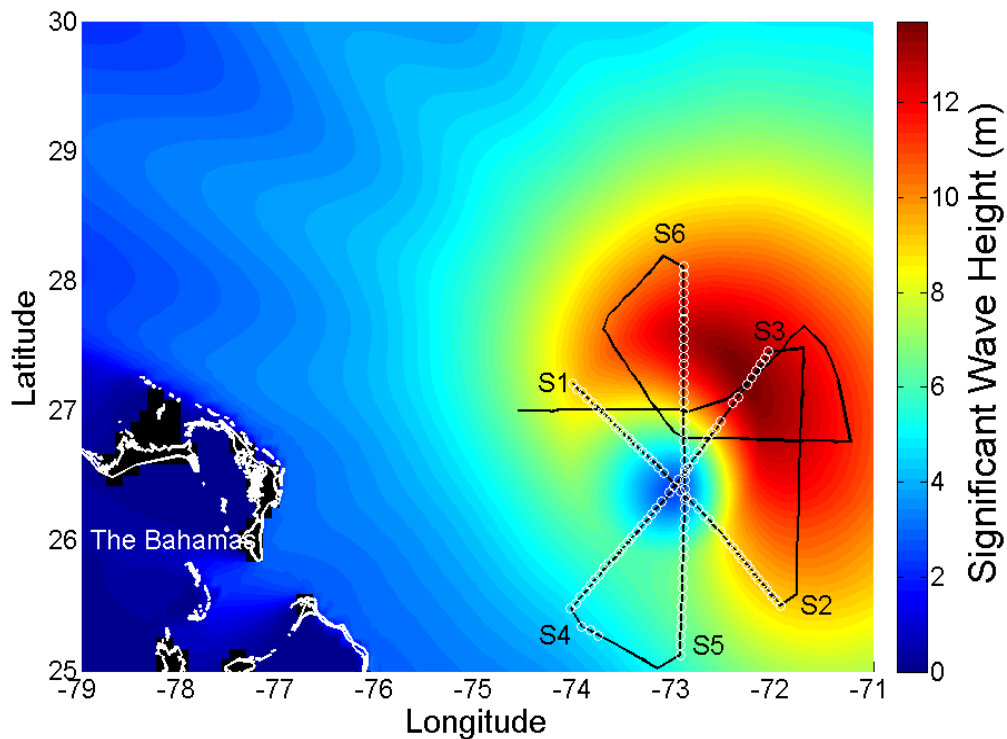


Figure 6. The color map is a snapshot of the significant wave height in meters simulated by WW3 at time 24 August 1998 22:30 UTC. The black line with white markers represents the path of the NOAA aircraft that carries the SRA, that crossed the storm in a butterfly pattern from 20:29 24 to 01:37 25 UTC. The white dots represent data points used in the study. S1 to S6 represent positions of aircraft selected to identify the flight legs that are used to analyze the data shown in Figure 7.

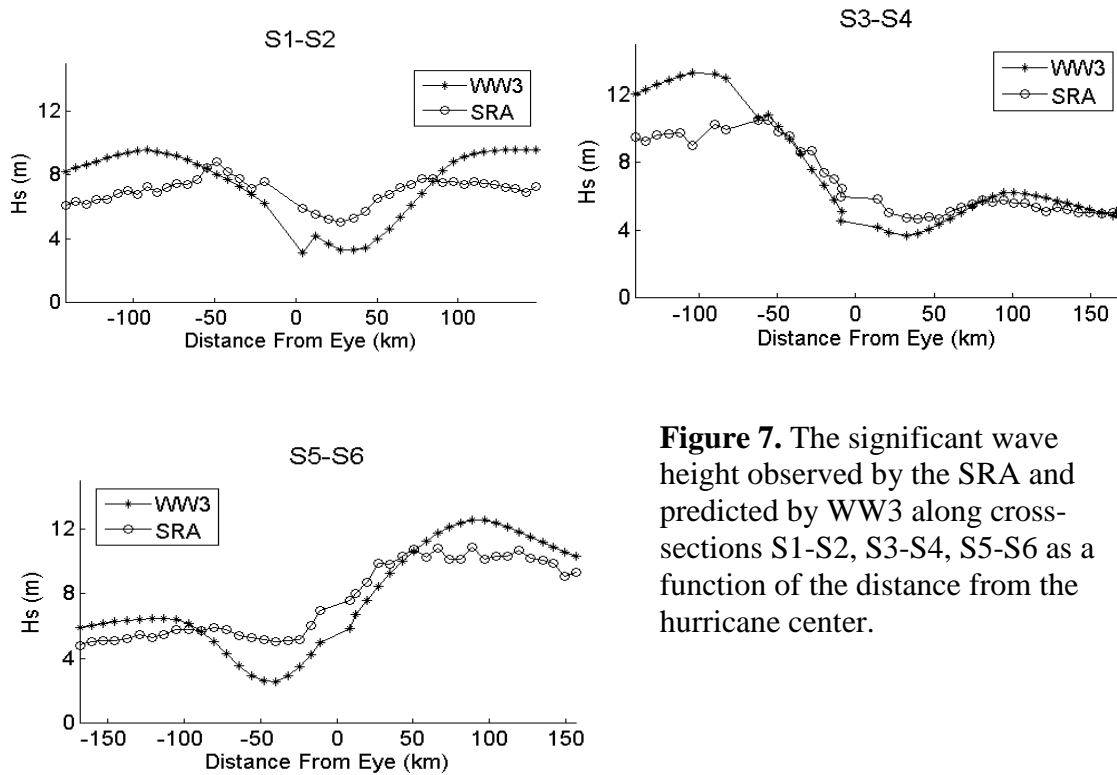


Figure 7. The significant wave height observed by the SRA and predicted by WW3 along cross-sections S1-S2, S3-S4, S5-S6 as a function of the distance from the hurricane center.

The red line of best fit in Figure 10 is for data points sampled at ocean depths less than 20 meters. The slope is 0.92 and has an intercept of 1.2 m. Despite the significant spread in the model data, the best fit slope is nearly one, thus WW3 overestimates the waves by 1.2 m on average in shallow water.

4. Discussion

The wave field generated by a moving hurricane is asymmetric with the highest waves in the front right section of the storm. In the open ocean, the significant wave height is overestimated by WW3 on the periphery of the storm and underestimated beneath the storm eye. Nonetheless, WW3 simulates the spatial variability of the wave field correctly.

The general overestimation of the significant wave height can be attributed to an overestimation of winds. However, one would expect that the uncertainties introduced by winds to be less influential in the shallow water than in the deep water. This is because in water depth of less than 30 m, wave heights are mainly depth controlled and the dissipation effects dominate. This agrees well with what we are seeing from our results. Hence, at least, the shallow water physics implemented in WW3 is working properly.

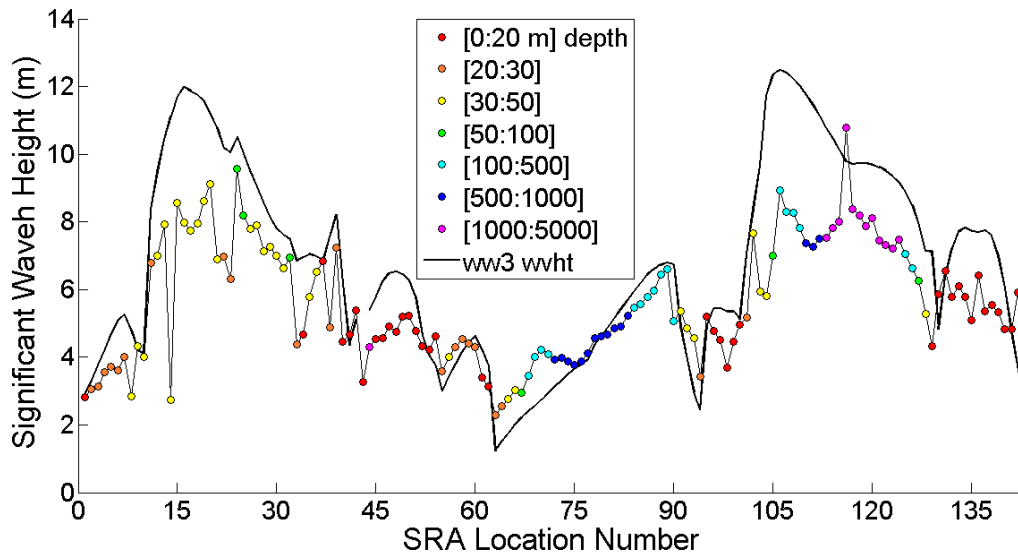


Figure 8. Significant wave height predictions (continuous line) of WW3 and SRA observations (color markers) at the locations of SRA data points. The colors represents the ocean depth at each location indicated by the legend. The SRA location number, x-axis, is shown in Figure 6.

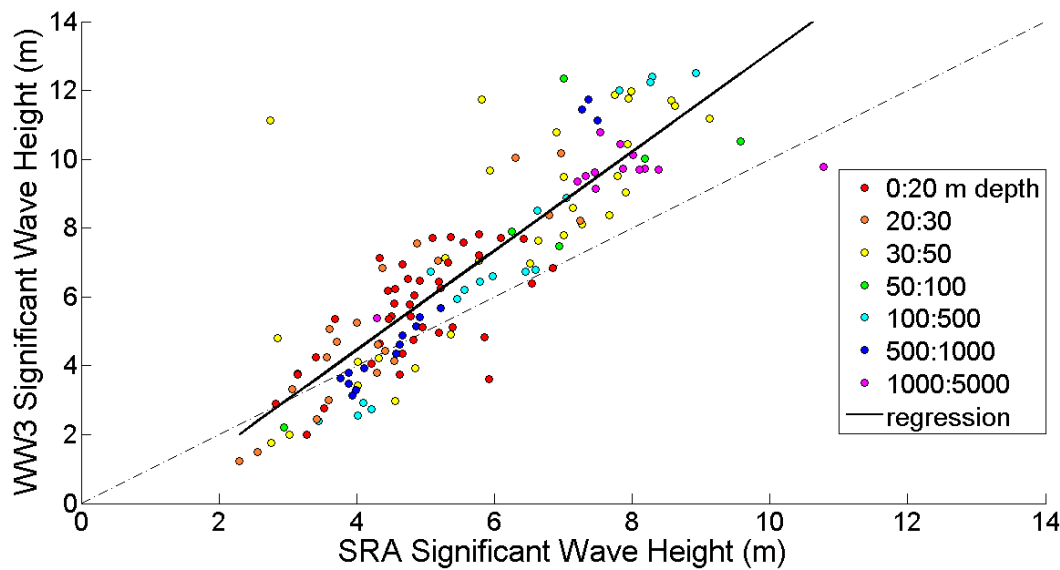


Figure 9. WW3 predictions and SRA observations are plotted against each other. The dashed line has a slope of 1. Any data point that falls on this line demonstrates a perfect agreement between WW3 and the SRA. The color of the markers indicate the ocean depth. The regression line is a least squares fit of all the data points having a linear form of $y=1.4x-1.2$

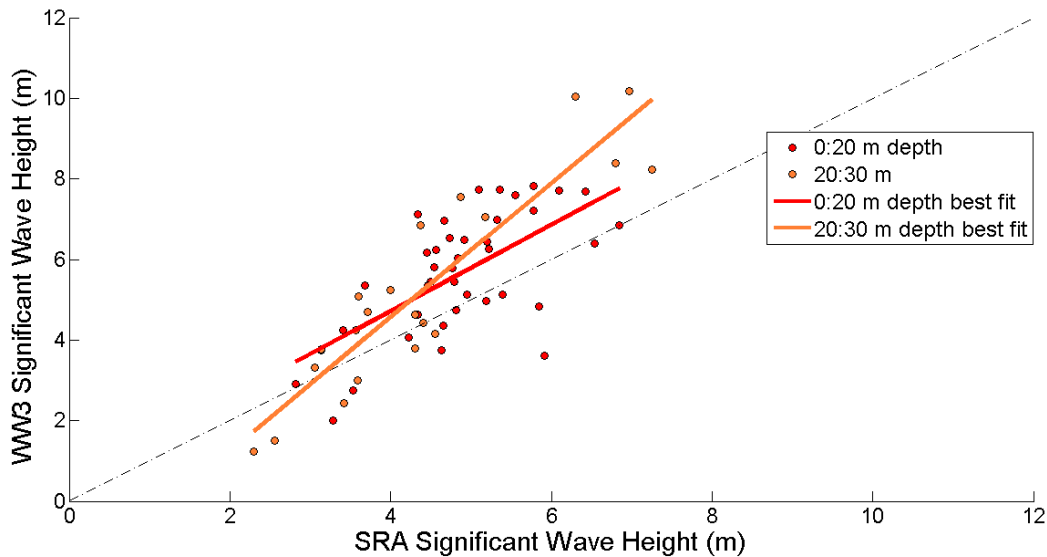


Figure 10. WW3 predictions and SRA observations plotted against each other, but with data points for ocean depths greater than 30 m omitted. The red line uses data points with ocean depths less than 20 m and has the form $y = .92x + 1.3$. The orange line is a best fit with form $y = 1.7x - 2.1$ using data points having ocean depths between 20-30 m.

For future study, several aspects can be considered:

1. Improve the wind forcing;
2. Include the effect of ocean currents in the wave simulations;
3. Compare other wave quantities, especially the wave spectrum; and
4. Evaluate performance of ST4 (the source terms used in current operational WW3).

4. Conclusions

WAVEWATCH III properly simulates the spatial variability of the waves in shallow water and the model results compare with the SRA data reasonably well. Although the maxima and minima generally align with the SRA measurements, WAVEWATCH III generally over estimates the significant wave height in shallow water.

Acknowledgments

I would like to thank the SURFO program for selecting me to be a Summer Undergraduate Research Fellow in Oceanography. Thank you to the National Science Foundation for funding my summer project as well as Xuanyu Chen and Isaac Ginis for mentoring me this summer.

References

- Fan Y., Ginis I., and Hara T. (2009), Numerical Simulation and Observations of Surface Wave Fields under an Extreme Tropical Cyclone, *Journal of Physical Oceanography*, 39, 2097-2117.
- Holland G. (1980), An Analytic Model of the Wind and Pressure Profiles in Hurricanes, *Monthly Weather Review*, 108, 1212-1218.
- Moon I., Ginis I., and Hara T. (2003), Numerical Simulation of Sea Surface Directional Wave Spectra under Hurricane Wind Forcing, *Journal of Physical Oceanography*, 33, 1680-1706.
- Wright C.W., Walsh E., Vandemark D., Krabill W.B. (2001), Hurricane Directional Wave Spatial Variations in the Open Ocean. *Journal of Physical Oceanography*, 31, 2472-2488.
- Tolman H. (2002). Development and Implementation of Wind-Generated Ocean Surface Wave Models at NCEP. *NCEP Notes*, 17, 311-333.
- Tolman, H.L. and D. Chalikov (1996). Source terms in a third-generation wind wave model. *Journal of Physical Oceanography* 26, (11): 2497-2518.

EXPLORING THE RELATIONSHIP BETWEEN GENETIC VARIANCE IN ComEC AND UPTAKE EFFICIENCY IN NATURAL TRANSFORMATION

Madison Flasco¹ and Ying Zhang²

¹Department of Biology, Otterbein University, Westerville, OH

²Department of Cell and Molecular Biology, University of Rhode Island, Kingston, RI

Abstract

Natural transformation is a process that allows for an organism to uptake free environmental DNA, a method of horizontal gene transfer, that serves as a mechanism for bacterial evolution. While the single stranded DNA transporter protein ComEC has been identified to be a core component of the transformation complex, little is known about the evolution of ComEC and how evolutionary variances are connected with transformation efficiency. This project aims to bridge this gap through computational studies of the *comEC* gene in complete bacterial genomes and experimentally study the constitutively competent model organism *Thermus thermophilus* via genetic modification. Computational analyses revealed the broad presence of ComEC proteins in 5,571 completely sequenced bacterial genomes. Identification of the domain structures of ComEC demonstrated variability among diverse phyla and revealed a small number that encode consistent structures of the ComEC proteins. Overall, genome size was found to be smaller in strains that lack ComEC or only contain the *Competence* domain and larger in strains containing the *Competence* domain and at least one additional domain. Using genetic modifications, a *comEC* knockout strain of *T. thermophilus* is being developed to study how the domain combinations in ComEC influences transformation efficiency. An expression vector was constructed to restore the wild type phenotype in the knockout strain. This will provide a foundation for future analysis of transformation efficiency with different ComEC types. Overall, the combined computational and experimental study of natural transformation and other mechanisms of horizontal gene transfer is critical to further understand bacterial ecology and evolution.

Proposal to the National Science Foundation Graduate Research Fellowship Program

(The rest of this section intentionally left blank)

OVERCOMING BARRIERS TO MOTIVATE COMMUNITY ACTION TO ENHANCE RESILIENCE

Courtney Hill, Tougaloo College
Donald D. Robadue, Jr., University of Rhode Island
Dawn Kotowicz, University of Rhode Island

This paper summarizes ongoing multi-method research seeking to improve community resilience by focusing on factors contributing to public policy change.

Natural disasters are becoming more frequent in the US and are increasingly attributed to climate change including sea level rise. Rhode Island, though the smallest state, has experienced and struggled to recover from a number of disasters within the living memory of some of its residents dating to the devastating Hurricane of 1938. The state's coastal management program has adopted increasingly detailed policies since the 1980s and hazard management plans at the state and local level have improved substantially since the 1990s. However, upgrading and implementing new methods of hazard mitigation for the evolving state policy have become a priority in recent years. The state has experienced more than four consecutive disasters between 2010 and 2013 in coastal and river systems. This raises questions regarding improvements to public policy: Are the policies and officials ready for the next disaster's impact? How can officials increase a community's resilience in the coastal zone and vulnerable flood plains? What roles do lived experience and new information play in improving policy?

The University of Rhode Island's Coastal Resource Center (CRC) is participating in a research project entitled "Overcoming barriers to motivate community action to enhance resilience", with the aim of understanding the factors that either foster or impede the adoption of better policies. The CRC research team is using a multi-method approach to retrospectively examine the relationship among major and minor storm events and hazards, scientific information about predicted future impacts and the adoption of mitigation measures at the local and state levels. The approaches include preparing a very detailed timeline of hazard events, storm impacts and policy responses dating back to the 1970s along with a comprehensive collection of studies and policy documents and press reporting of local and state responses to key events. In addition, a social network analysis was used to map out the organizations and individuals who have participated in advocating as well as resisting proposals to increase community resilience. The project team also looked for trends in decision making and development patterns in the data base of 41,000 permits issued by the State Coastal Resources Management Program in the period 1971 -2016.

One element of this research, led by the lead author, focused on preparing a case study of a specific major storm event and ensuing disaster known locally as the Great Floods of 2010, which affected the Pawtuxet River and the surrounding watershed, located in the middle portion of the state. The objective of this task was to apply the methods employed in the overall project to determine whether policy actually changes after such a major hazard event. A timeline was constructed to add details on this event. In 2010, a portion of Rhode Island became victim to a flood. The municipalities of Cranston, West Warwick, and Warwick were severely flooded in what was labeled locally as the storm of the century. In Warwick, a city of 81,500 people, the wastewater treatment facility became flooded and severely disrupted. The facility became unable to operate during this period; leading the mayor to announce to use less water because the raw wastewater would be discharged into the Pawtuxet river. Expensive and extensive damage affected the Warwick Wastewater Treatment Facility, the Warwick Shopping Mall and critical sections of Interstate 95. The floods of 2010 became an important turning point for the treatment facility. The City of Warwick took full advantage of the numerous grants and funding available to investigate the cause of the flooding and various methods to prevent such a catastrophic impact in the future. Different municipalities along the Pawtuxet River began to enhance their flood mitigation efforts and ultimately build their disaster resilience.

To build resilience, the state must first identify the barriers in the current hazard plan. One of the barriers discovered through the timeline analysis was the fact that, before 2010, the local hazard mitigation plan did not include the Warwick Wastewater Treatment Facility. After the flood, the wastewater authority was required to participate in state level storm hazard simulation events, planning, and hazard mitigation activities, with the overall goal to improve the preparation, response, and recovery efforts of the authority to minimize the impact of the next disaster.

A social network analysis was also used to find connections and relationships in before and after the 2010 floods. One of the key actors identified in the initial scan was Janine Burke, the director of the Warwick Wastewater Treatment Facility. The network analysis shows that she became a key figure in local and state hazard mitigation efforts and has been able to communicate the story of Warwick's effective longer range response to the storm event.

After identifying key people who appeared to be leaders in the policy changes, interviews were conducted with Janine Burke and William Patenaude, a representative on the state's Wastewater Operator Certification board and a leader in the state's wastewater treatment program. Burke explained her personal role during and after the floods, elaborating on mistakes and responses that led to another way to address and avoid future storm impacts such as composing a hazard plan. William Patenaude provided information and reports on how the state was implementing new resilience efforts inspired in part by the manner in which Warwick took advantage of the

experience to become better prepared. The material gathered from the interviews aligned with the information found in the timeline.

Based on the success of this case study, the CRC research team will further analyze other local experiences to uncover whether they too have enabled local or state reforms that can improve hazard resilience.

Funding for this research was provided in part by Department of Homeland Security Coastal Resilience Center of Excellence led by The University of North Carolina at Chapel Hill (UNC-CH).

Courtney Hill
Coastal Resource Center
University of Rhode Island
220 South Ferry Road
Narragansett, RI 02882
Courtney.hill_16@yahoo.com
(601) 519-2291

MULTI-ENVIRONMENTAL GROWTH ASSESSMENT PLATE: A NEW METHOD OF CONDUCTING TEMPERATURE DEPENDENT GROWTH EXPERIMENTS WITH PHYTOPLANKTON

Kierra Jones¹, Stephanie Anderson², and Tatiana Rynearson²

¹Tougaloo College, Tougaloo, Mississippi

²Graduate School of Oceanography, University of Rhode Island, Narragansett, Rhode Island

Corresponding author: Kierra Jones (kierratj@gmail.com)

Running head: M.E.G.A Plate Analysis

Key Point:

- The overwhelming diversity of phytoplankton has led to the formation of innovative measures of conducting temperature dependent experiments.

Key Index Words:

Phytoplankton, temperature, climate change, thermal reaction norm

Abstract

Climate change has been greatly attributed to the increased levels of greenhouse gases, such as atmospheric carbon dioxide produced by the use of fossil fuels. As a result, Narragansett Bay temperatures have increased 1.5°C-2.5°C since the 1960s. As temperatures increase, the metabolism of phytoplankton increases, but it is unknown how different species respond to increasing temperatures. Increased metabolism can affect global cycles of carbon, nitrogen, and phosphorus. To understand the effects of temperature on phytoplankton we conducted growth rate experiments on isolates collected from the Narragansett Bay spring bloom in March to note the thermal limits and identify how different species respond to different temperatures. Previously, these experiments required multiple incubators set to different temperatures, which is very time intensive and relies on having extensive incubator resources. We propose a method that includes creating a Multi-Environmental Growth Assessment (M.E.G.A.) plate that would allow growth rate experiments to occur at various temperatures in one setting. We tested the M.E.G.A. plate using diatom species collected from Narragansett Bay identified using molecular techniques. A statistical analysis of M.E.G.A. plate data was done to verify a temperature gradient and consistency. The data indicate that the M.E.G.A. plate will allow for analysis of several strains simultaneously under multiple thermal conditions. The data demonstrate the diversity of diatom thermal responses from species isolated during a winter/spring bloom in Narragansett Bay.

(The rest of this section intentionally left blank)

Nutrient Cycling of the Southern Ocean during Late Summer

Amanda Love¹ and Rebecca S. Robinson²

¹Department of Chemistry, Lake Superior State University, Sault Ste Marie, Michigan

²University of Rhode Island Graduate School of Oceanography, Narraganset Rhode Island, USA

Corresponding author: Amanda Love (alove1@lssu.edu)

Running head: Nitrogen uptake across Southern Ocean

Key Points:

- Nitrate consumption increases toward tropics
- Assimilation is the dominant process controlling nitrate isotopes
- A secondary source of nitrate from Subtropics is identified

Keywords: Nitrogen, nitrate assimilation, Southern Ocean, isotopic ratios, Rayleigh fractionation

Abstract

The Southern Ocean plays a critical role in the exchange of carbon dioxide (CO₂) between the atmosphere and the oceans. High biological productivity during the summer is one way that CO₂ is drawn into the ocean. Tracking the year-round nutrient cycles of this environment including nutrient abundance, production, and consumption will help us to understand the role of the Southern Ocean biological pump in regulating atmospheric CO₂. Water samples were collected along 170° W in the Southern Ocean on research expedition NBP17-02 between January and March 2017. NB17-02 transected the entire Southern Ocean, including the Polar Antarctic Zone, Polar Frontal Zone, and Subantarctic Zone. We measured nitrogen and oxygen isotopes of nitrate ($\delta^{15}\text{N}$ and $\delta^{18}\text{O}$) and nitrate concentrations. Isotope analyses were made following the denitrifier method, where the bacterium, *Pseudomonas aurefaciens*, transfers nitrate nitrogen and oxygen present in the sample to nitrous oxide. The nitrous oxide produced was analyzed through gas chromatography-isotope ratio mass spectrometry to quantify the $\delta^{15}\text{N}$ and $\delta^{18}\text{O}$ present in the original nitrate molecule. The equatorward increase in both the $\delta^{15}\text{N}$ and $\delta^{18}\text{O}$ of nitrate reflects the progressive consumption of nitrate away from the major Southern Ocean upwelling zone. As predicted, the relationship between the nitrate concentration and $\delta^{15}\text{N}$ and $\delta^{18}\text{O}$ values in the Southern Ocean follows the Rayleigh model. Deviations from the Rayleigh prediction for $\delta^{15}\text{N}$ change indicate the introduction of Subtropical water in northern most stations.

(The rest of this section intentionally left blank)

Submerged Paleo-Shorelines as Markers of Vertical Deformation around Lake Azuei, Haiti

Oliver Lucier

Rice University, Houston TX, USA (ofl1@rice.edu).

Key Points:

- Lake Azuei lies in the eastern extension of the Enriquillo-Plantain Garden Fault, which is one of two transform faults that defines the North American – Caribbean plate boundary.
- A former shoreline, now submerged ~ 10 m beneath the lake level of Lake Azuei, was mapped.
- Analyses were applied to determine whether that formerly horizontal paleo-shoreline has been deformed by tectonic activity.
- Radioisotope dating is applied to sediment samples from the lake; resulting dates will constrain the age of that paleo-shoreline – and thus constrain the possible rate of tectonic deformation in the region.

Key Index Words:

Haiti, Transform fault, Bathymetry, Sediment core, Paleo-Shoreline, Subbottom profiling (CHIRP) sonar, Tectonic deformation

Abstract

Lake Azuei, one of the largest lakes in the Caribbean (10×23 km), is found at the eastern end of the Cul-de-Sac basin in Haiti. The southern half of Lake Azuei is located on the eastern extension of the Enriquillo-Plantain Garden fault zone. That fault marks part of the Caribbean plate's northern boundary and relative motion across its trace combines shortening and strike-slip components. Over the last fifteen years the water level of Lake Azuei has risen a remarkable ~ 5 m, submerging villages, cultivated land, and roads, thus greatly disrupting the livelihoods of nearby inhabitants. Using new (2017) and existing (2013) sub-bottom seismic profiling (CHIRP) data we compiled an updated and improved bathymetric map of Lake Azuei that revealed young folds protruding from the lakebed. Additionally, the CHIRP data highlighted several paleo-shorelines. We imaged a paleo-shoreline at ~ 5-m depth, resulting from the recent lake level rise, as well as a prominent paleo-shoreline at ~ 10 m, suggesting a long period where the lake level was ~ 10 m lower than today's level. This ~ 10-m paleo-shoreline is covered by a thin ~ 20-cm sediment layer, suggesting that it was only submerged centuries to millennia ago. We are currently testing if this ~ 10-m paleo-shoreline has been slightly warped away from horizontality due to tectonic activity. Lastly, using three core samples collected from the lakebed, we are radiometrically dating the sediment layers present in the lake to determine their ages and the rate of sedimentation. Grain-size and microscopic analysis will constrain the composition and depositional environments of the sediment layers.

1. Introduction

On January 12, 2010 a magnitude 7.0 earthquake occurred on the Léogâne fault in southwest Haiti [Calais et al., 2010]. This earthquake caused terrible damage and loss of life in Haiti, especially in the densely populated region around the capital Port-au-Prince. Since the earthquake, a concerted effort has been made to analyze seismic risk in Haiti in order to better prepare for future earthquake threats [Calais et al., 2010; McHugh et al., 2011; Prentice et al., 2010]. One key area where research into seismic risk in Haiti is currently underdeveloped is Lake Azuei, one of the largest lakes in the Caribbean (10 km × 23 km), which is located on the populous Cul-de-Sac plain only 20 miles from Port-au-Prince. This paper examines how paleo-shorelines produced by the fluctuating level of Lake Azuei can be a useful tool to quantify vertical deformation and thus assess the level of seismic risk.

2. Geologic Setting

The Léogâne fault, on which the 2010 M7.0 earthquake occurred, conjoins with the Enriquillo-Plantain Garden Fault (EPGF), which is one of two major transform faults demarcating the boundary between the Caribbean plate and the North American plate. The EPGF travels through the southern peninsula of Haiti, along the southern edge of the capital city of Port-au-Prince, and across the Cul-de Sac basin before potentially terminating at Lake Azuei, the largest lake in Haiti [Mann et al., 1995; Smithe and Calais, 2016; St Fleur et al., 2015]. Lake Azuei is located in an active and complex geologic setting, where the southern and northern portions of Hispaniola are not only sliding past each other in a sinistral (left-lateral) motion, but are simultaneously squeezing together, resulting in transpressional tectonics: figuratively squishing the central Cul-de-sac basin, on which Lake Azuei is located (*Figure 1*). One of the goals of this research was to investigate how this transpressional motion is accommodated in the central region of Haiti, and one of the most effective tools for performing this investigation was to apply marine seismic methods in Lake Azuei.

3. Paleo-shorelines

Past studies have shown how paleo-shorelines can be used to determine the amount of vertical deformation caused by tectonic activity in a given area [e.g., Cormier et al., 2006; Polonia et al., 2004; Jara-Munoz et al., 2017]. Paleo-shorelines, when they are formed, are horizontal features. If one can trace a paleo-shoreline in a tectonically active area, one can determine whether or not that paleo-shoreline has been vertically deformed by measuring its depth at many separate locations, and testing to see if these measurements vary geographically. If the depth measurements of the paleo-shoreline do vary spatially, they document vertical deformation. Then, by radiometrically dating the paleo-shoreline and surrounding geologic layers, one could calculate the associated rate of deformation. The rate of deformation, which provides information on how often a large earthquake is likely to occur in a particular area and what type of earthquake it might be (strike-slip, thrust, or combined), is an important factor for determining seismic risk.

GPS measurements, which record instantaneous deformation rate, and historical records dating back to the sixteenth century demonstrably show that a destructive earthquake should be expected at the Enriquillo-Plantain Garden Fault this century (e.g.

Symithe et al., 2013). It is imperative to accurately quantify the historical deformation rate along the EPGF so that decision makers can better predict the timeframe when this earthquake might occur. By measuring the vertical deformation of Lake Azuei using varying depth measurements of a paleo-shoreline, one can calculate some past deformation rates that will allow for a more accurate characterization of seismic risk along the EPGF.

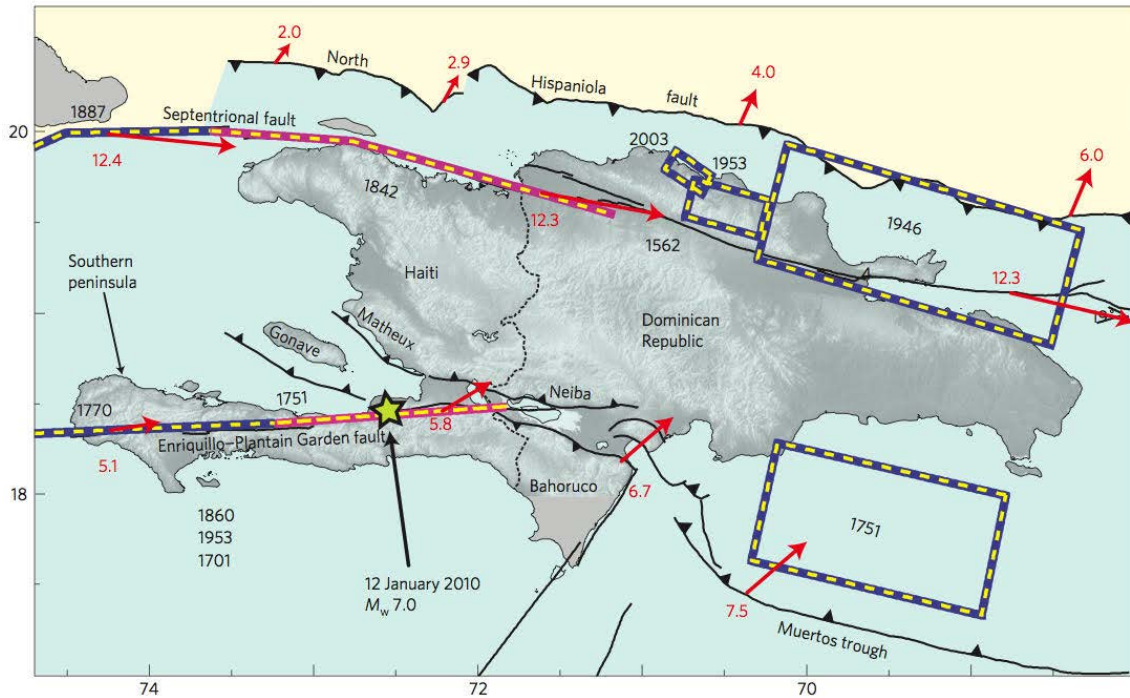


Figure 1: Major tectonic structures across Hispaniola, including the left-lateral Enriquillo-Plantain Garden Fault and Septentrional Fault [after Calais et al., 2010]. Black numbers indicate dates of historical earthquakes, and their estimated ruptures are indicated with either a colored line (strike-slip) or a colored box (thrust). Arrows indicate estimates of relative velocities (in mm/yr) across the plate boundaries.

4. Fluctuating Lake Level

Another startling component of the geographic nature of Lake Azuei is the fact that over the last fifteen years the water level has risen ~ 5 meters [Monaktian et al., 2017]. Lake Enriquillo, a neighboring lake in the Dominican Republic, has risen ~ 10 m. Neither lake has an outlet to the sea nor are they connected to each other, making their levels particularly sensitive to variations in hydrographic conditions. The cause for these large lake level changes is believed to be increased precipitation due to climate change. The presence of many paleo-shorelines in Lake Azuei shows that past climatic events have controlled the lake level. As part of this study, we also identified a paleo-shoreline above the current lake level, at ~ 28 m, using satellite imagery. This paleo-shoreline is recognizable as a subtle change in vegetation. Its elevation corresponds precisely to the lowest elevation around the lake (~28 m), suggesting that it formed when the lake rose another ~7 m above its present level and spilled over its sill point. These observations

point to the fact that the lake level has a large and variable range and that it may continue to rise.

This lake level rise has had serious effects upon the economy and livelihoods of the local Haitian population [Kushner, 2017; Grogg, 2012]. The rising lake has submerged acres of arable land, and even swallowed whole villages: displacing large numbers of people and disrupting local enterprises. It is necessary for local authorities to understand the causes and rate of lake level change to help mitigate its socio-economic impacts. Although the slow rate of vertical tectonic deformation might contribute only minimally to this sudden rise in lake level, a future earthquake beneath the lake would only worsen the challenges facing the surrounding population.

5. Materials and Methods

5.1 CHIRP Data analysis

In January of 2017, a three-week expedition to Lake Azuei gathered subbottom profiling (CHIRP) data, multichannel seismic reflection data, and three sediment cores [Cormier and Sloan, 2017]. This on-going research project is funded by the National Science Foundation and is fully collaborative with scientists at the State University of Haiti. The CHIRP profiles provide information not only on water depth but also on sediment stratigraphy from ten to twenty meters below the lakebed (*Figure 2*).

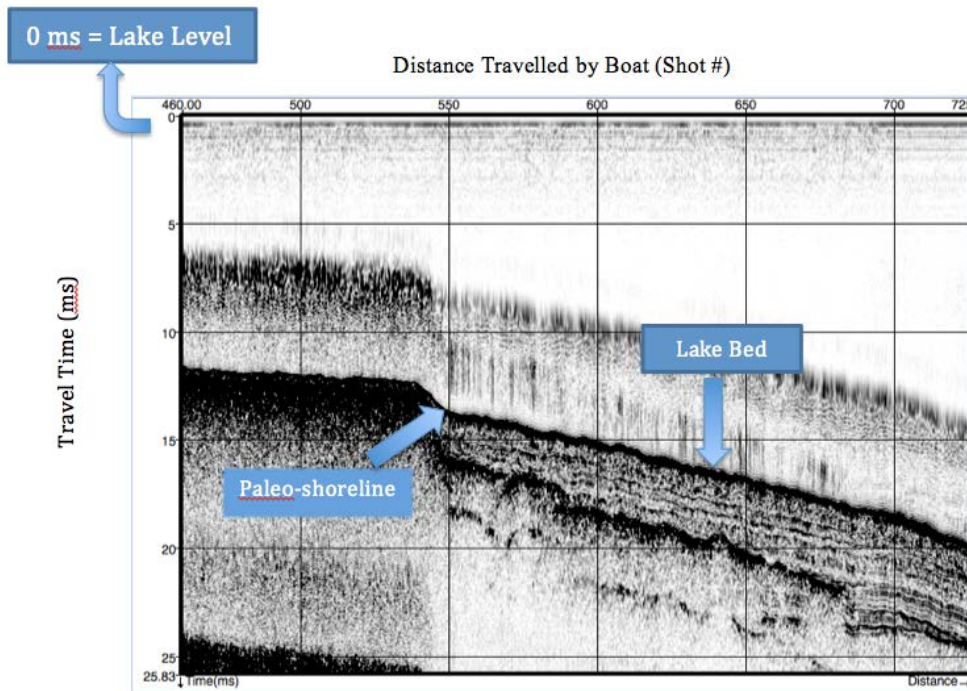
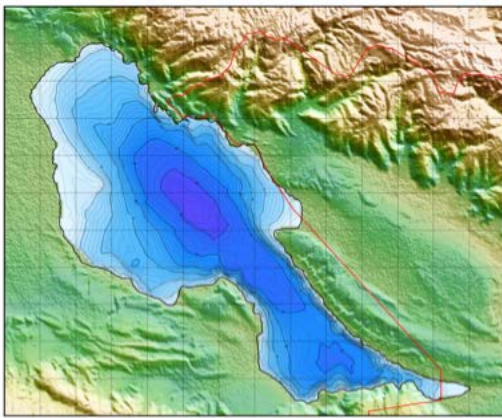


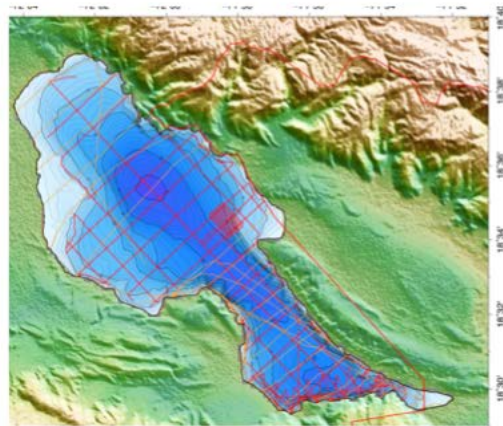
Figure 2: CHIRP profile across the ~10 m deep paleo-shoreline. The vertical axis is two-way travel time and is labeled in millisecond; 1 ms corresponds to approximately 75 cm water depth (assuming 1500 m/s for the speed of sound in water).

To interpret the CHIRP data recorded in Haiti, we utilized the free seismic interpretation software OpendTect (<https://www.opendtect.org>). OpendTect is a powerful

interactive software that can display seismic profiles in 2D and 3D viewer modes and allows one to digitize "seismic horizons" (geological boundaries). Most importantly, it shows the profiles in their 3-dimensional contexts in relation to each other, allowing operators to visualize the field relations between key geological features. On these profiles, the lakebed was easily recognizable (*Figure 2*). We digitized the lakebed on every profile and compiled these horizons into an updated bathymetric map of Lake Azuei using the map-producing free software GMT (<https://www.soest.hawaii.edu/gmt/>). These new data improve on the previous soundings of the lakebed collected in 2013. These 2013 data were removed from the new compilation and the updated bathymetric map showed that the deepest part of the lake is actually 5 m shallower than previously thought (30 m instead of 35 m deep), and is shifted toward the northwest (*Figure 3*).



Bathymetric map compiled from the raw sounding data generously provided by M. Piasecki, City College - CUNY. These data were collected in 2013 (Monaktian et al. 2017)



Updated bathymetric map. Orange lines indicate the tracks from the 2013 survey of M. Piasecki. Red lines are from the 2017 survey (this study).

Figure 3: Comparison of bathymetric maps

5.2 Paleo-shoreline Identification

Using the CHIRP profiles, we were able to identify features indicative of paleo-shorelines. The most prominent of these telltale features was the "shoreline angle", which was identifiable due to the distinct change in slope of the lakebed, which was created by wave erosion at the former shoreline (*Figure 4*).

Another noticeable feature that we used to identify paleo-shorelines was the observation that below the paleo-shoreline, on the lake-ward side of the paleo-shoreline the CHIRP sonar signal penetrates much further thereby revealing the stratigraphy of the geologic layers. On the other hand, the part of the profile above the paleo-shoreline, on its landward side, revealed little to no penetration below the lakebed (*Figure 2*). These combined observations are consistent with the hypothesis that during the time period when the paleo-shoreline was formed, the lake level must have held relatively constant for a length of time sufficient to produce a shoreline angle. This would have allowed a sandy or rocky beach to form on the landward side of the paleo-shoreline thus forming a

hard and almost impenetrable seismic reflector, while in comparison sediments such as silt and mud would have deposited on the lake-ward side of the paleo-shoreline, thus creating an easily penetrable, much softer, seismic reflector. Lastly, on some of the paleo-shorelines we imaged, we found that on the landward side of the paleo-shoreline pick, the lakebed appeared bumpy and irregular in the seismic profile, indicative of a rougher, uneven surface, whereas on the lake-ward side of the paleo-shoreline the lakebed was a much smoother reflector in the seismic profile.

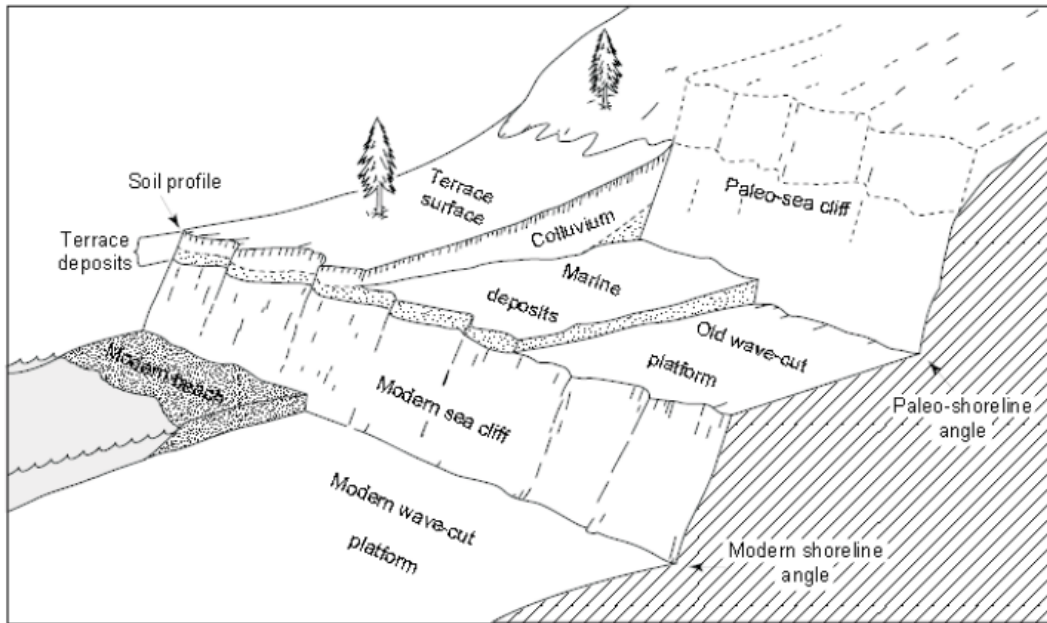


Figure 4: Main morphological features generated at a shoreline (after Weber, 1983). The “shoreline angle” is generally the easiest feature to identify across a paleo-shoreline.

Another feature that added complexity to the task of picking the paleo-shoreline was that a thin layer of sediment (~ 20 cm) had been deposited above the paleo-shoreline after it had been submerged. This layer of sediment was especially pronounced on the landward side of the paleo-shoreline on the CHIRP profiles. In order to account for this sedimentation, we picked the paleo-shorelines below this layer of sediment.

We were able to identify several paleo-shorelines: a paleo-shoreline at ~5-m depth (we assume this to be the paleo-shoreline from around 15 years ago before the recent and abrupt lake level rise), a paleo-shoreline at ~10 m, which was very clearly defined and present on every one of our seismic profiles, and in a few profiles only, two paleo-shorelines at much deeper depths (~22 m and ~35 m). We chose to focus on the ~10-m shoreline for our analysis of vertical deformation given that it was the most prominent and prevalent of all the paleo-shorelines we identified.

Using OpendTect, we took precise picks of the ~10-m paleo-shoreline on each seismic profile where we could clearly identify it. We then performed screen captures of the ~10-m paleo-shoreline on all the profiles on which it was located. The exact depth and x and y coordinates of our picks were read directly from the screen and this information was compiled in an Excel table. The next step will be to plot the depth measurements versus their geographic locations around the perimeter of the lake in order

to objectively assess if there exist systematic trends that could be attributed to tectonic deformation. There exists a degree of uncertainty for all of our paleo-shoreline picks. Picking the paleo-shoreline measurements was a subjective process. One estimate of the uncertainty will be the standard deviation of the curve derived from the plot of depth measurements-versus-distance around the lake. Another way to evaluate error will be for other investigators working on this project to repeat the measurements and then compare their results with our own. For now, we estimate that measurement errors do not exceed more than ~20 cm.

5.3 Sediment Core Processing

The analysis of the three sediment cores collected from the lakebed of Lake Azuei required a series of steps. The three cores were spliced and opened (*Figure 5*).



Figure 5: Opened core. Ruler alongside the core indicates cm below top of the core.

We extracted samples from each core for radiometric dating. For each core we sampled material every centimeter for the top 10 cm, then every other centimeter between the ten- and 20-cm depth marks, and lastly every 5 cm from the 20-cm mark onwards until the bottom of the core. We took samples from all three cores: LA17-BC01-1 A which measured 56 cm, LA17-BC02-1 A which measured 87 cm, and LA17-BC01-3 A which measured 74 cm. We chose to utilize the isotope ^{210}Pb for radiometric dating due to the fact that the only previous coring sample of Lake Azuei had suggested very high sedimentation rates, around 6 mm/year [Eisen-Cuadra et al., 2013]. This high sedimentation rate meant that our relatively short cores could only sample a few hundred years of sediment accumulation; therefore, we chose a radioactive isotope that decays with a half-life of 22 years. Using CHIPR profiles, we could trace a sediment layer presumably deposited at the same time that the paleo-shoreline was forming, through the exact location where we cored. It is possible that ongoing radiometric dating of the cores, and particularly of the layers corresponding to the paleo-shoreline will reveal the age of the paleo-shoreline. Even if we are not able to date the exact layer corresponding to the paleo-shoreline we will still be able to determine local sedimentation rates, which we

could extrapolate to the paleo-shoreline layer. This information would allow us to quantify the rate of vertical deformation below Lake Azuei.

As well as radiometric ^{210}Pb dating we took smear slides of all the sediment layers in the three cores, which will be examined under a microscope and photographed. Next, we drew diagrams representative of each core that show to scale all of the different sediment layers, and we provided written descriptions of each sediment layer including color identifications. We also took grain size samples at the same depth intervals as the radiometric dating samples.

6. Preliminary Results

The research performed for this study has revealed several significant, thought-provoking, and beneficial results that point to a need for further research of the Lake Azuei area. First, using the CHIRP data we were able to compile an improved bathymetric map of Lake Azuei, which revealed a shallower depocenter depth and different depocenter locations. It also highlights a very flat lakebed ($< 0.1^\circ$ slope) surrounded by steep slopes ($\sim 5^\circ$). Additionally, using the $\sim 10\text{-m}$ paleo-shoreline that we identified, we are in the process of determining the amount of vertical deformation affecting this region, if any (*Table 1*). Any trend, or lack thereof, will allow us to form a hypothesis about the amount, rate, and location of vertical deformation below Lake Azuei.

Table 1: Measurements of $\sim 10\text{-m}$ paleo-shoreline

Paleo-shorelines 13 ms depth			
CHIRP Line #	X (UTM, m)	Y (UTM, m)	depth (m)
304	179840	2057922	9.575
305	186899	2056880	10.543
306	187379	2054964	10.768
401.001	184985	2060309	10.062
402	185486	2059774	9.404
403	180544	2053713	9.495
403.001	186209	2059339	9.912
500	186769	2056097	9.648
603	186982	2057015	10.103
604	186908	2057840	9.939
902	186738	2056690	9.985
903	186676	2056611	9.965
904	186652	2056490	10.18
905	186616	2056377	9.957
906	186830	2055986	9.518
913	193711	2048553	9.585
914	193838	2048460	9.768
918.001	190558	2047424	9.764
918.001	189384	2047121	9.799

The majority of the results of this research are still forthcoming. Analysis is continuing and further results will be presented at the 2017 fall meeting of the American Geophysical Union in the papers of Cormier et al., 2017 and Sloan et al. 2017.

8. Conclusions

The use of paleo-shorelines to determine vertical deformation is a growing field of study that allows geophysicists to identify vertical deformation of a lakebed or seafloor. For this specific study we successfully identified and catalogued a paleo-shoreline in Lake Azuei, Haiti. We are currently in the process of analyzing our paleo-shoreline data to discover any trends indicative of tectonic deformation.

Acknowledgments

Oliver Lucier was supported by a Summer Undergraduate Research Fellowship in Oceanography (SURFO) (National Science Foundation REU grant # OCE-1460819). This project is financed by the U.S. National Science Foundation under grants EAR-1624583 and EAR-1624556. During this summer research internship, I have had the immense pleasure of working with Dr. Milene Cormier, a research scientist at the Graduate School of Oceanography, and Casey Hearn, a doctoral candidate at the Graduate School of Oceanography. Both have been instrumental to this research. Additional thanks go to R. Patrick Kelly for his help with ^{210}Pb dating.

References

- Calais, E., A. Freed, G. Mattioli, F. Amelung, S. Jonsson, P. Jansma, S.-H. Hong, T. Dixon, C. Prepetit, and R. Momplaisir, 2010. *Transpressional rupture of an unmapped fault during the 2010 Haiti earthquake*, *Nature Geoscience*, 3, 794-799.
- Cormier M.H., H. Sloan, and the Lake Azuei Project Team, *Lake Azuei Project, Haiti; Field Report*, <https://www.projectlakeazuei.org>, January 9 - February 3, 2017.
- Cormier, M.H., H. Sloan, D. Boisson, B. Brown, K. Guerrier, C.H. Hearn, C.W. Heil, R.P. Kelly, J.W. King, P. Knotts, O.F. Lucier, R. Momplaisir, R. Stempel, S.J. Symithe, S.M.J. Ulysse, and N.J. Wattus, 11-15 December 2017, *Signature of Transpressional Tectonics in the Holocene Stratigraphy of Lake Azuei, Haiti: Preliminary Results From a High-Resolution Subbottom Profiling Survey*, Fall Meeting of the American Geophysical Union, Session T047, abstract # 259609, New Orleans.
- Cormier, M.H., L. Seeber, C.M.G. McHugh, A. Polonia, M.N. Çagatay, Ö. Emre, L. Gasperini, N. Görür, G. Bortoluzzi, E. Bonatti, W.B.F. Ryan, and K.R. Newman, 2006. *The North Anatolian fault in the Gulf of Izmit (Turkey): Rapid vertical motion in response to minor bends of a non-vertical continental transform*, *J. Geophys. Res.*, 111, doi:10.29/2005JB003633, B04102.
- Eisen-Cuadra, A., A. Christian, E. Dorval, B. Broadaway, J. Herron, R. Hannigan, 2013. *Metal geochemistry of a brackish lake: Etang Saumâtre, Haiti*, *Medical Geochemistry*, 149-166.

- Grogg, P., 31 August 2012, *Rapidly rising lake levels threaten trade on Dominican-Haiti border*, The Guardian, <https://www.theguardian.com/global-development/2012/aug/31/lake-levels-threaten-dominican-haiti-border>.
- Jara-Muñoz, J. & Melnick, D., 2015, *Unraveling sea-level variations and tectonic uplift in wave-built marine terraces, Santa María Island, Chile*. *Quat. Res.* **83**, 216–228.
- Kushner, J., 3 March 2016, *The Relentless Rise of Two Caribbean Lakes Baffles Scientists*, National Geographic, <http://news.nationalgeographic.com/2016/03/160303-haiti-dominican-republic-lakes/>.
- Mann, P., F.W. Taylor, R.L. Edwards, and T.L. Ku, 1995, *Actively evolving microplate formation by oblique collision and sideways motion along strike slip faults: An example from the northwestern Caribbean plate margin*, *Tectonophysics*, 246, 1–69.
- McHugh, C.M., L. Seeber, N. Braudy, M.H. Cormier, M.B. Davis, J.B. Diebold, N. Dieudonne, R. Douilly, S.P.S. Gulick, M.J. Hornbach, H.E. Johnson*, K.R. Mishkin, C.C. Sorlien, M.S. Steckler, S.J. Smithe, and J. Templeton, Offshore sedimentary effects of the 12 January 2010 Haiti earthquake, *Geology*, 39, 723-726, 2011.
- Monaktian, M., M. Piasecki, and J. Gonzalez, 2017. *Development of Geospatial and Temporal Characteristics for Hispaniola's Lake Azuei and Enriquillo Using Landsat Imagery*, *Remote Sensing*, 9(6), 510; doi:10.3390/rs9060510.
- Polonia, A., L. Gasperini, A. Amorosi, E. Bonatti, G. Bortoluzzi, M.N. Çagatay, L. Capotondi, M.H. Cormier, N. Görür, C.M.G. McHugh, L. Seeber, 2004, *Holoceneslip rate of the North Anatolian Fault beneath the Sea of Marmara*, *Earth Planet. Sci. Lett.*, 227, 411-426.
- Prentice, C.S., P. Mann, A. J. Crone, R. D. Gold, K. W. Hudnut, R. W. Briggs, R. D. Koehler, and P. Jean, Seismic hazard of the Enriquillo–Plantain Garden fault in Haiti inferred from palaeoseismology, *Nature Geoscience*, DOI: 10.1038/NGEO991, 2010.
- Saint Fleur, N., N. Feuillet, R. Grandin, E. Jacques, J. Weil-Accardo, Y. Klinger, 2015. *Seismotectonics of southern Haiti: A new faulting model for the 12 January 2010 M7.0 earthquake*, *Geophysical Research Letter* 10.1002/2015GL065505 AGU Publications, 10273-10281.
- Sloan, H., M.H. Cormier, D. Boisson, B. Brown, K. Guerrier, C.H. Hearn, C.W. Heil, L. Hynes, R.P. Kelly, J.W. King, P. Knotts, O.F. Lucier, R. Momplaisir, R. Stempel, S.J. Smithe, S.M.J. Ulysse, and N.J. Wattrus, 11-15 December 2017, *Subbottom seismic profiling survey of Lake Azuei, Haiti: Seismic signature of paleo-shorelines in a transpressional environment and possible tectonic implications*, Fall Meeting of the American Geophysical Union, Session T047, abstract # 259797, New Orleans.
- Smithe, S., E. Calais, JS. Haase, A.M. Freed, and R. Douilly, Coseismic Slip Distribution of the 2010 M 7.0 Haiti Earthquake and Resulting Stress Changes on Regional Faults, *Bulletin*

of the Seismological Society of America, 103(4), 2326–2343, doi: 10.1785/0120120306, 2013.

Symithe, S., and E. Calais, 2016. *Present-day shortening in Southern Haiti from GPS measurements and implications for seismic hazard*, *Tectonophysics*, 679, 117-124.

Weber, G.E., 1983, *Geological investigation of the marine terraces of the San Simeon region and Pleistocene activity on the San Simeon fault zone, San Luis Obispo County, California: Menlo Park, Calif.*, technical report to U.S. Geological Survey under Contract 14- 08-00001-18230, 66 p.

Spectral Analysis and Characteristics of a Variety of Open Ocean Regions

Nicholas Piskurich¹, Peter Cornillon², Baylor Fox-Kemper³, Brodie Pearson³

¹ Department of Civil and Environmental Engineering and Earth Sciences, University of Notre Dame, Notre Dame, Indiana

² University of Rhode Island Graduate School of Oceanography, Narragansett, Rhode Island

³ Department of Earth, Environmental, and Planetary Sciences, Brown University, Providence, Rhode Island

Corresponding author: Nicholas Piskurich (npiskurich2@gmail.com)

Key Points:

- Spectral analysis is a powerful time-series analysis method used in physical oceanography
- Comparing directional spectral slopes can aid in describing submesoscale ocean dynamics
- Spectral analysis can communicate where large-scale circulation models are failing to simulate submesoscale physical processes

Key Index Words: spectral analysis, structure functions, ocean dynamics, turbulence, circulation models

Abstract

Spectral analysis of oceanographic data is an ubiquitous, powerful tool used in examination of macroscale and microscale turbulence regimes, ocean dynamics, and submesoscale processes. Specifically, the shape of the power spectra concomitant with open ocean characteristics (i.e. satellite-derived sea surface temperatures (SST), velocity components) can aid in understanding ocean dynamics in a specific region. Via data from the Advanced Very High Resolution Radiometer (AVHRR) and Moderate Resolution Imaging Spectroradiometer (MODIS) and more recent high quality data from the Visible Infrared Imaging Radiometer Suite (VIIRS), spectral analysis can be performed on spatial scales of 1 to hundreds of km. Currently, spectral analyses exist for regions at significantly coarser spatial resolution of ~10 km. However, spectra from the AVHRR and VIIRS SST fields (both 750 and 375 m) can be calculated and analyzed for many open ocean regions with spectral slopes that vary temporally, spatially, and seasonally with a finer spatial resolution of 4 km. Data collected from the VIIRS Moderate Resolution Band was processed using algorithms developed in MATLAB involving the Fast-Fourier Transform (FFT) method for clear 256-pixel along-scan and along-track cloud-free segments from 1 degree \times 1 degree to 20 degree \times 20 degree. An ensemble average of segments was conducted seasonally and regionally to develop a global climatology of spectral slopes in the 5 to 50-km range. Spectral results were compared to the results obtained from the container ship *Oleander* in the 5 to 50-km range. Global temporal, zonal, and meridional spectral slopes via the FFT method have been obtained for each of the four seasons and the year of 2011-2012. Other statistically significant quantities have been calculated, including the global variances for each of the variables temperature, salinity, and velocity components U, V, and W. The spectral slopes are compared to their closely related structure functions in order to analyze similarities and differences between the two methods. Overall, power spectra can be analyzed with these structure functions as a mechanism to communicate how global ocean general circulation models may have problems with properly simulating and depicting

submesoscale turbulence and other small-scale physical processes. As a result, in-depth analysis and a comprehensive understanding of turbulence regimes, intermittency, isotropy and anisotropy, homogeneity, sources of energy and enstrophy, and ocean dynamics can be obtained.

1. Introduction

Oceanographers have long debated how and in what way energy can be transferred and dissipated to smaller scales, particularly the submesoscale. Currently, many oceanographic and atmospheric models exist in order to simulate physical processes at the mesoscale (>100 km) down to the order of 1 km to the millimeter scales. However, many of these models make assumptions about physical processes at the submesoscale (10 km – 100 km), which leaves a large gap in oceanographers' understanding and comprehension of turbulent processes that are dominant at these scales and how energy is transferred and dissipated throughout the submesoscale. General circulation models (GCMs) exist in order to simulate physical and thermodynamic processes at work within the atmosphere or the global ocean, but a lack of knowledge of and a number of assumptions about small-scale turbulence and other submesoscale processes render these climate and atmospheric models inaccurate and incomplete.

In order to fully comprehend and determine these large-scale circulation models, a greater knowledge must be obtained about the nature of turbulent processes in the atmosphere and the oceans (McCaffrey et. al 2015). A comprehensive understanding of the physics in the submesoscale is crucial to determining the relationship between small-scale turbulence and large-scale oceanic and atmospheric circulation models. One of the major working hypotheses about turbulence theory is whether energy fluxes and transfers in the submesoscale are controlled by internal waves and unbalanced motions or whether there is a significant contribution from motions that are geostrophic (i.e. where the pressure gradient force is balanced by the Coriolis effect) (Callies and Ferrari 2013). Many of these high-resolution ocean GCMs as well as numerical weather prediction models (NWP) which model physical processes make assumptions about the physics at work at scales that are smaller than the model-grid spacing; this is known as sub-grid scale parameterization (Schloesser et. al 2015). However, recent numerical model work as well as observational results show that these physics at small scales, particularly the submesoscale, which is not resolved in these global ocean GCMs, cannot have such assumptions and are, in fact, rich in structure and physical turbulent processes (Schloesser et. al 2015). Moreover, the processes that are at work within the submesoscale may have a critical part in these large-scale circulation models due to their impact on air-sea interactions and vertical motions and redistributions throughout the water column. Most of the advanced high-resolution models utilize sub-grid schemes that are chosen for their stability and simplicity, but some of these models and their schemes are unreliable in terms of simulating physical phenomena whereas other numerical sub-grid schemes are incompatible with observations. One of the major goals of this project is to quantify and qualify where these sub-grid schemes are inconsistent with many of the submesoscale physical characteristics and processes and how spectral analyses can be used to pinpoint where large-scale circulation models are failing to simulate or quantify submesoscale physics due to these numerical assumptions at small scales.

Turbulence at the mesoscale and the submesoscale has been studied via the use of spectral analyses and structure function analyses for many decades (McCaffrey et. al 2015). Previous spectral analyses had only utilized a spatial resolution of ~ 10 km, but with the use of the VIIRS sea surface temperature (SST), velocity components, and salinity observations in the 375-m and 750-m bands, spectral analyses

can be obtained with a spatial resolution of ~ 4 km. Additionally, observations of the ocean surface indicate that spectral behavior at scales larger than ~ 1 km can be differentiated from submesoscale or small-scale turbulence (McCaffrey et. al 2015). Spectral analyses can yield statistically significant information and can exhibit variations globally, regionally, temporally, and spatially such that information about turbulence regimes, homogeneity, isotropy, and energy and enstrophy cascades can be obtained. Moreover, these power spectra can aid in understanding where a numerical subgrid model is failing to produce reasonable and realistic small-scale turbulence. Once these analyses of power spectra are completed, results will be compared to in situ data gathered from the Oleander as well as observational data analyzed via the use of second-order and higher-order structure functions. These structure functions yield much of the same information as power spectra with the exception that they are more useful with irregular data series or gaps in data. Overall, power spectra can be used as excellent evaluation tools for understanding the similarities and differences between observational satellite and in situ data as they compare to MIT's ECHO II model that is used in this study. Analyses of power spectra can also be used as powerful metrics for understanding where large-scale and mesoscale circulation models are failing to properly depict submesoscale features and processes and where these subgrid schemes and their assumptions are unnecessary and inaccurate in terms of properly examining turbulent regimes and energy dissipation schemes at small scales.

2. Materials and Methods

In order to perform spectral analyses and develop a global climatology of spectral slopes for the entire region, algorithms in MATLAB had to be developed to obtain spectral slopes at the ocean surface. First, the global ocean surface had to be gridded in a field split into an 18×13 grid with equivalent $20^\circ \times 20^\circ$ squares. Each degree of these squares is equivalent to approximately 111 km with approximately 4 km per pixel of the grid indices (Figure 1).

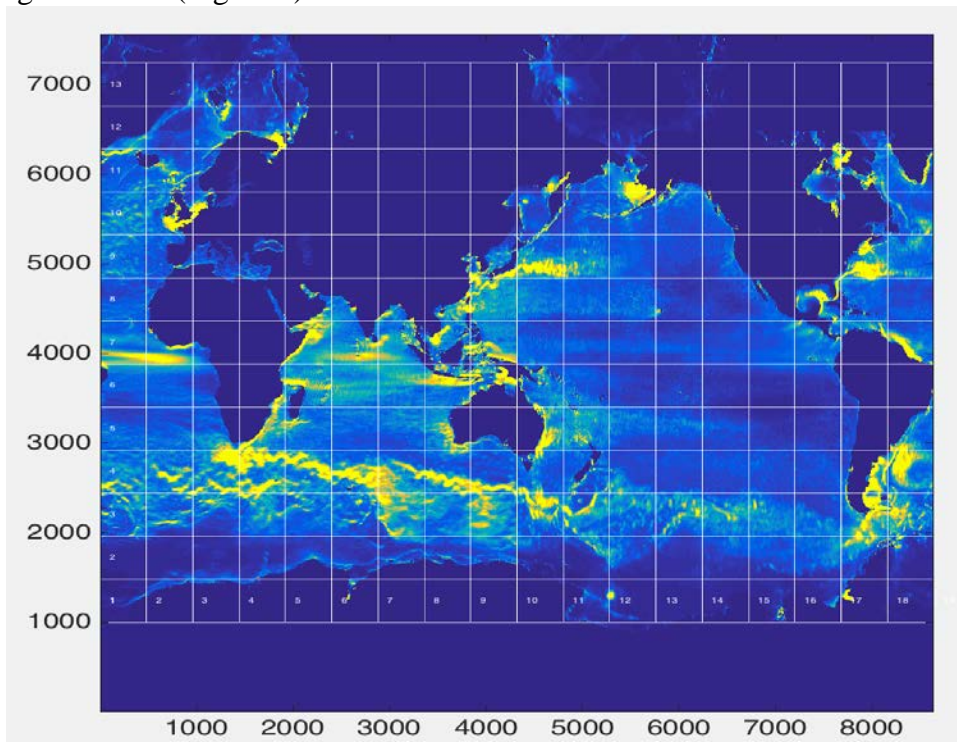


Figure 1. Global SST super grid broken into $20^\circ \times 20^\circ$ squares with corresponding indices.

After breaking up the global ocean surface into this super grid of $20^\circ \times 20^\circ$ squares, power spectral densities were obtained for a particular $1^\circ \times 1^\circ$ square within each of the $20^\circ \times 20^\circ$ squares. Because each degree is equivalent to 111 km, and there are approximately 4 km per pixel, each $1^\circ \times 1^\circ$ square had about 625 (or 25×25) pixels. In order to obtain the power spectra for each of these $1^\circ \times 1^\circ$ squares, a longitudinal and latitudinal value was hardwired into the algorithm as a starting point for each analysis. Following this, an upper and lower longitudinal and latitudinal point was implemented in order to center the analyses on a particular $1^\circ \times 1^\circ$ region. Next, a loop was implemented in order to pass through all of the longitude and latitude points while maintaining the process within the uppermost and lowermost longitudinal and latitudinal values to stay within the global grid parameters. Once the algorithm was situated in the center of a particular $1^\circ \times 1^\circ$ region, the algorithm estimated all of the places within the region where there was not a statistical value, and the number of spectra was calculated for all of the places where there existed a statistical value.

In order to calculate the power spectral density for each of the $1^\circ \times 1^\circ$ regions in the temporal dimension, a loop was created to obtain the power spectra for each of the four seasons and the entire calendar year of 2011-2012. Another algorithm was established to physically calculate the power spectral density for each of the $1^\circ \times 1^\circ$ squares by inputting sample spacing, the temperature of the sample, and various preprocessing elements, which included a normalization factor, a detrending factor, a windowing factor (i.e. a Blackman window), a demeaning factor, and an averaging factor in order to average the elements of input temperature sections. The output of this algorithm contained the wavenumber, the temperature sections following preprocessing, the Fast Fourier Transform (FFT) of the input temperature section, the power spectral density (PSD), and the phase of the PSD components. For the temporal dimension, it was established within the algorithm to start on the date June 1 (perpetual calendar day 87) and end on May 31 (perpetual calendar day 446). By doing this, a FFT was performed about each season by establishing a loop; once the power spectral densities were obtained for each of the four seasons, the seasons were then concatenated together to obtain the PSD values for the entire year of 2011-2012. After obtaining the PSD values and demeaning and detrending the data, an ensemble average was implemented as well as a calculation to find the slopes, intercepts, and figures of merit for each of the PSD that were plotted in frequency space with log-PSD on the y-axis and log-wavenumber on the x-axis.

In order to calculate the PSD values in the meridional and zonal directions, three of the super grid elements (i.e. $20^\circ \times 20^\circ$ squares) had to be concatenated together. For the zonal direction, three horizontal super grid elements were concatenated together whereas in the meridional direction, three vertical super grid elements were concatenated together. A loop was then implemented again to define the uppermost and lowermost longitudinal and latitudinal values. After this, the algorithm for finding the meridional and zonal spectra situated a point in the center of the three concatenated $20^\circ \times 20^\circ$ squares. For the meridional direction, a FFT was conducted about every longitudinal line within the $1^\circ \times 1^\circ$ squares for 128 pixels (64 above and 63 below) which was centered around a mid-latitude point defined as average of the upper and lower latitudinal values; for the zonal direction, the FFT was conducted about every latitudinal line within the $1^\circ \times 1^\circ$ squares for 128 pixels (64 to the left and 63 to the right) which was centered around a mid-longitude point defined as the average of the upper and lower longitudinal values. For the meridional and zonal directions, it was noted that there was a breakpoint in most of the spectra close to the wavenumber and wavelength corresponding to about 25 km, so lines of code were implemented within the algorithm to calculate two first-order polynomials (i.e. two lines of best fit) to compensate for this breakpoint in energy for most of the graphs of PSD. An ensemble average of PSD values for each of the four seasons and entire calendar year was conducted followed by

obtaining two slopes, two intercepts, and two figures of merit for the two lines of best fit for the meridional and zonal power spectral densities. The first line of best fit was from 2-20 on the log-wavenumber axis; the second line of best fit was established from 25-45 on the log-wavenumber axis.

3. Results

Algorithms developed in MATLAB yielded a global climatology of power spectral density values and their corresponding spectral slopes in the temporal dimension and in the spatial dimensions (i.e. meridional and zonal). These algorithms were successful in inputting variables (i.e. SST, velocity components (U,V,W), and salinity) and a vector of longitudinal and latitudinal super grid elements in order to output a wavenumber, ensemble averaged PSD, two first order polynomials, two intercepts, and two figures of merit. Two slopes and two first order polynomials were chosen to account for the noticeable breakpoint in energy level at a particular wavenumber or wavelength around $\sim 20 - 25$ km for both the meridional and zonal spectra. Figure 2 shows typical power spectra for the meridional and zonal directions plotted on a log-PSD versus log-wavelength.

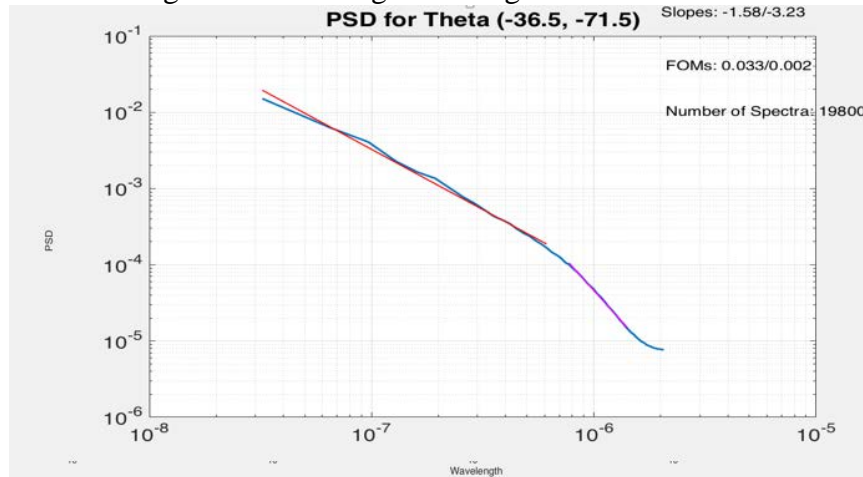


Figure 2. Typical power spectra graph with slopes, FOMs for given lon. and lat. points.

Two slopes and two first-order polynomials were necessitated for the meridional and zonal power spectra graphs due to the noticeable breakpoint in the energy spectrum at a characteristic wavelength and wavenumber. This breakpoint in energy is generally accounted for by a steeperslope (the magenta line in Figure 2), where more energy is being added to the spectrum due to overdamping from the model. Some of these graphs showed a ‘hook’ upwards near the rightmost region of the graph at higher wavenumbers and lower wavelengths due to the fact that not enough energy was being added to the spectrum, which could be accounted for because of underdamping of the model.

These graphs were obtained for each of the temporal, meridional, and zonal power spectra by performing a FFT about each of the $1^\circ \times 1^\circ$ boxes and moving vertically and horizontally along the super grid in order to obtain a global climatology of power spectra and their corresponding slope values for each of the four seasons and the entire year of 2011-2012. Figures 3, 4, 5, and 6 compare the global meridional and zonal spectral slopes for the variable U for each of the four seasons and the year of 2011-2012.

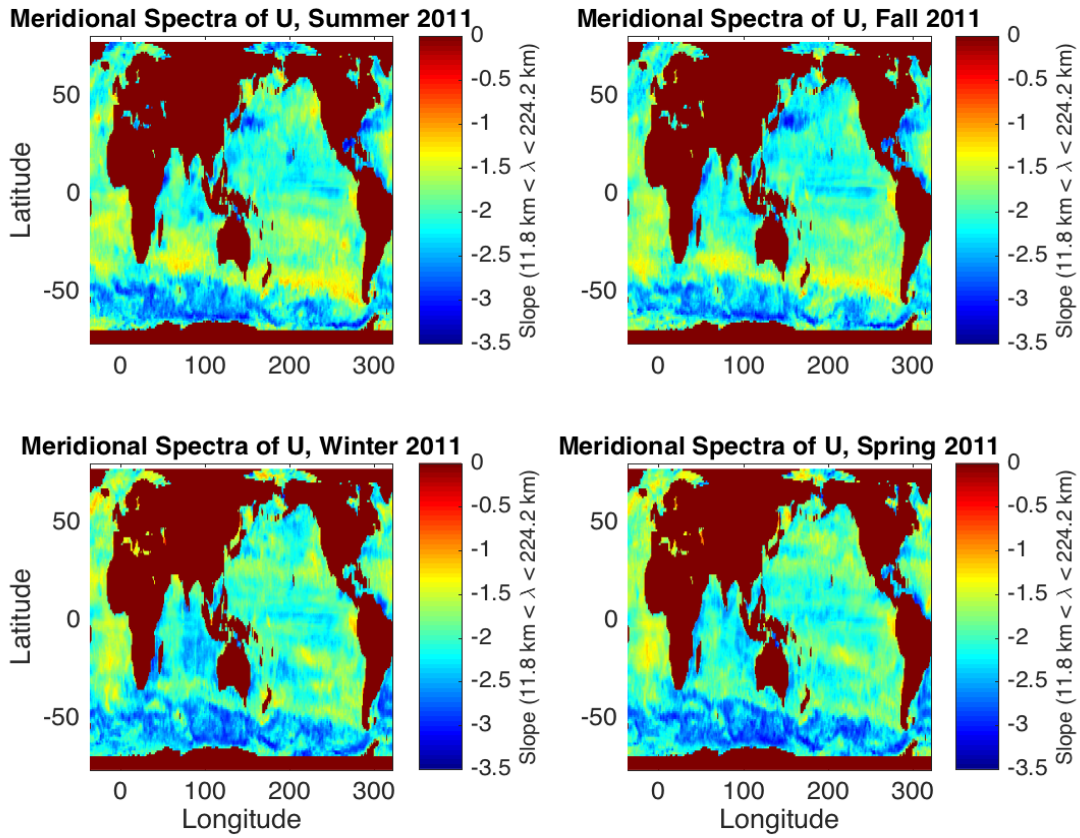


Figure 3. Seasonal meridional spectral slopes for U, 2011-2012.

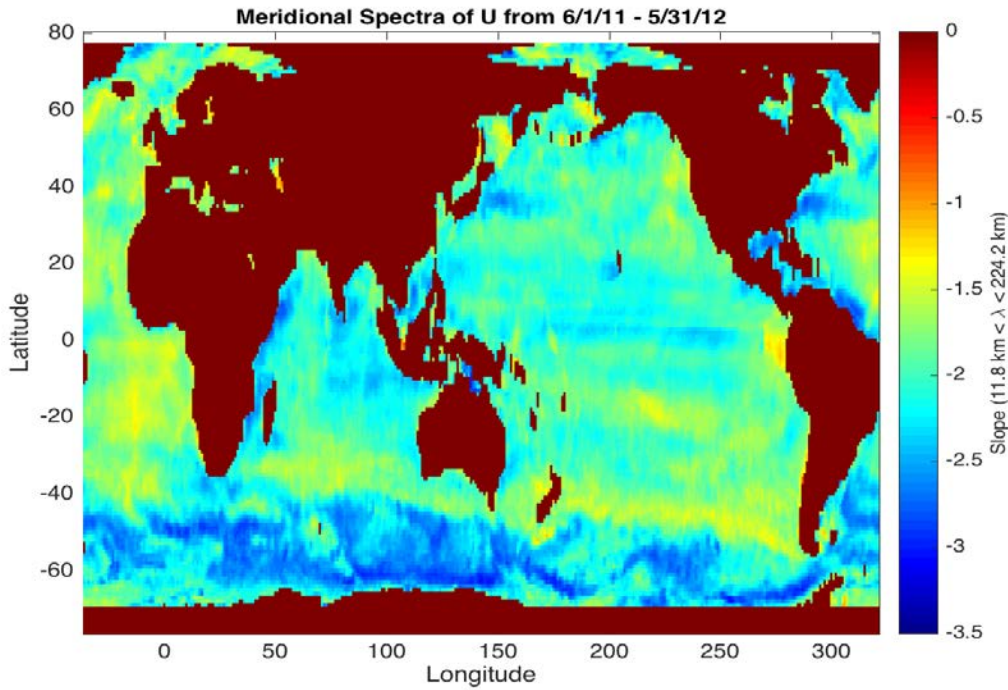


Figure 4. Annual meridional spectra for U, 2011-2012.

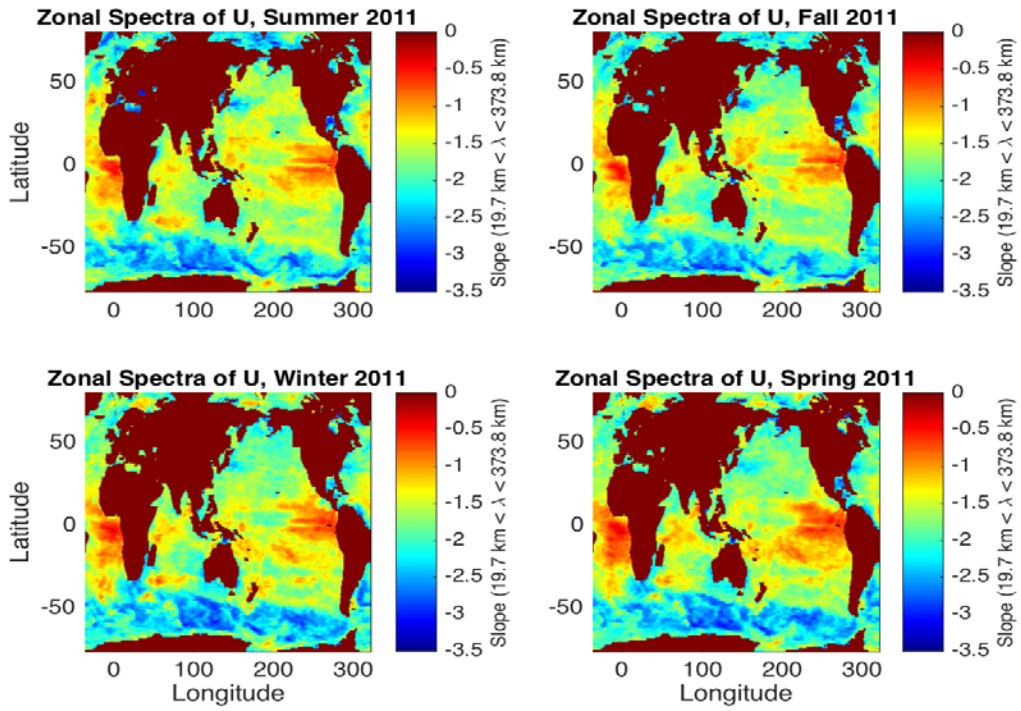


Figure 5. Seasonal zonal spectra for U, 2011-2012.

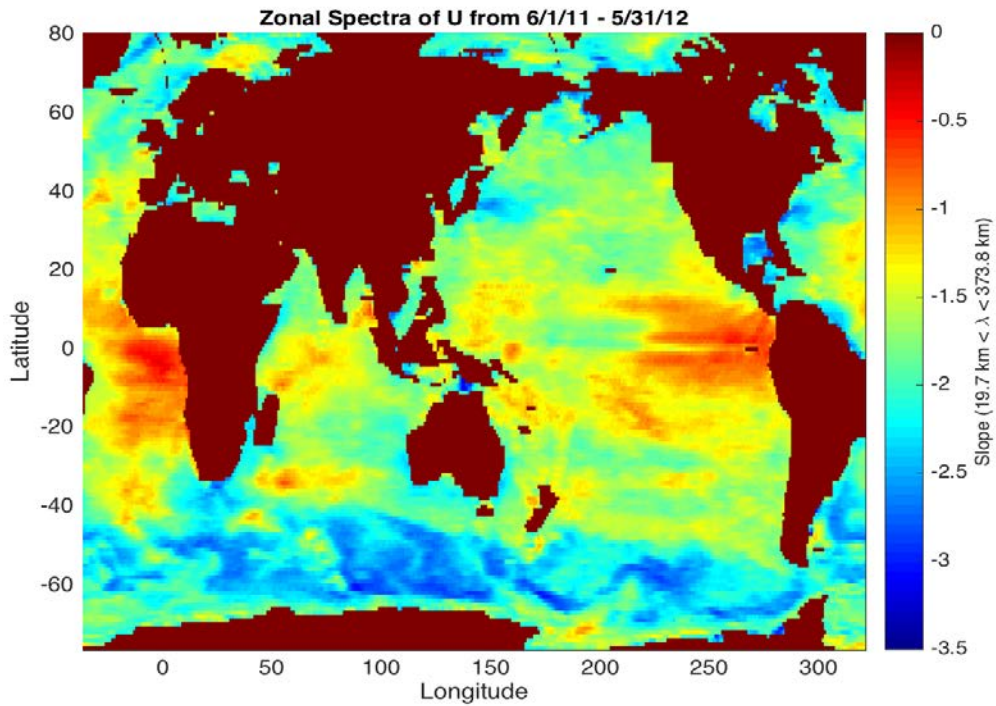


Figure 6. Annual zonal spectra for U, 2011-2012.

These graphs were obtained for every variable, U, V, W, sea-surface temperature, and salinity for each of the three dimensions: temporal, zonal, and meridional. Particularly, for the spatial dimensions for a given variable, the zonal and meridional spectra were compared to analyze whether the magnitude of the variable being measured was altered based on the direction of measurement. If the magnitude of the variable in question varies by direction of measurement (i.e. zonal, meridional), this is referred to as anisotropy. However, if the magnitude of the spectral slopes does not vary significantly by direction of measurement, this is known as isotropy.

4. Discussion

For the meridional spectral slopes of U, there were noticeably steeper spectral slope values in the Antarctic Circumpolar Current (ACC) region than in the equatorial or mid-latitudes regions, and the same trend held true for the zonal spectral slope values for U. Moreover, for the meridional spectral slopes for U, there appeared to be steeper slopes (i.e. more energy) near the Western-boundary currents (i.e. the Kuroshio, Gulf Stream, Agulhas) whereas the spectral slopes were significantly less energetic and less steep near dynamically quiescent areas such as the Sargasso Sea. In terms of comparing the zonal to the meridional spectral slopes for the U variable, the zonal spectral slopes for U tended to be shallower in the equatorial and mid-latitude regions, which led to the condition of anisotropy for a significant portion of the globe. However, in the ACC region, the spectral slopes for meridional and zonal U tended towards -3, which indicated a fair amount of isotropy in these regions. Additionally, seasonal variations were present within each of the meridional and zonal U spectral slopes; in general, steeper slopes tended to be observed in the ACC region for the winter and spring in the meridional and zonal U spectral slopes.

For the meridional slopes of V, steeper slopes were again seen in the ACC region as well as the regions near the Western-boundary currents whereas shallower slopes were present in the mid-latitude regions. In terms of seasonal variations in spectral slopes, the values of the meridional spectral slopes for V tended to be shallower in the mid-latitude regions during the summer and fall whereas the meridional slopes tended to be steeper in these regions in the winter and spring; moreover, meridional spectral slopes tended to be steeper in the winter and spring in the ACC region and Southern ocean. When comparing the meridional and zonal spectral slopes for V, slopes tended toward -3.5 and tended to be steeper in the zonal spectral slopes than in the meridional spectral slopes, which led to fairly anisotropic behavior. Additionally, spectral slopes tended toward -2 in the equatorial region for the zonal spectra whereas spectral slopes were closer to -5/3 for the meridional spectra of V, which lent itself to a fairly anisotropic behavior. Annually, the zonal spectra tended to be much steeper than the zonal spectra in the equatorial, ACC region, and mid-latitudes, and for both the meridional and zonal spectra, slopes characterized by a -3 value tended to be in the regions near the Western-boundary currents.

A similar analysis was conducted for each of the five variables that were analyzed in this study: U, V, W, temperature, and salinity. In general, for each of the five variables, slopes tended to be steeper in the energetic regions such as the Gulf Stream and other western boundary currents. Moreover, slopes varied considerably in the equatorial regions for each of the five variables whereas slopes tended toward -3 near the ACC and the Southern Ocean regions in general for each variable. Overall, there are approximately four values of slopes that are of considerable importance in describing geostrophy, energy transfers, and submesoscale and mesoscale turbulence regimes: k^{-1} , $k^{-5/3}$, k^{-2} , k^{-3} . In general, energy is transferred through interactions involving nonlinear turbulence and is eventually dissipated by

viscosity (Wang et. al 2009). Each of these values of spectral slopes represents a different turbulence regime and particular energy transfer at work at the mesoscale or submesoscale (Figure 7).

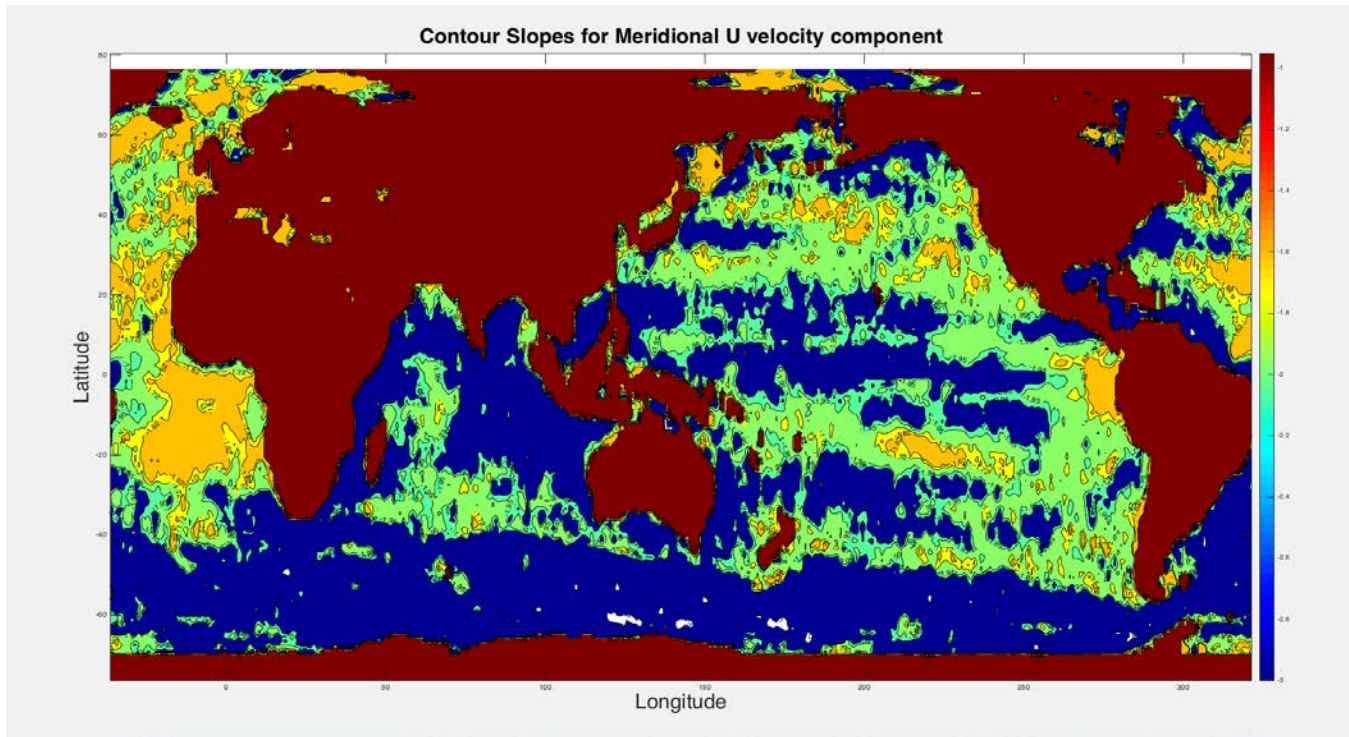


Figure 7. Contour slopes for meridional U velocity component.

The colors correspond to the following slope values: blue is a slope of -3 , lime green is a slope of -2 , between the yellow and orange hues is a slope of $-5/3$, and red is a slope of -1 . Energy generally cascades to smaller scales following the Kolomogoroff law of slope of $k^{-5/3}$, and this is generally typical of three-dimensional homogeneous isotropic turbulence (McCaffrey et. al 2015). In general, areas where a three-dimensional homogeneous turbulence regime is present include a portion of the equatorial regions and sporadic regions throughout the mid-latitudes. Moreover, due to energy and enstrophy (mean-square vorticity) constraints, energy is transferred to larger scales (inverse cascade) whereas enstrophy is transferred in the opposite direction to smaller scales (enstrophy cascade), and these occur in a turbulence regime of two-dimensional turbulence (McCaffrey et. al 2015). A slope of $k^{-5/3}$, the Kolomogoroff law, is generally true for inverse cascades whereas a slope of k^{-3} is true for the enstrophy cascade to smaller scales. In general, a slope of k^{-3} , indicative of the enstrophy cascade, tends to appear in the Southern Ocean and ACC region and intermittently throughout the equatorial and even mid-latitude regions. Particularly, this seems the dominant energy regime present throughout much of the global oceans where enstrophy is transferred to smaller scales. Finally, a velocity spectrum of k^{-2} is consistent with the surface quasigeostrophic turbulence theory, and is dominant in the equatorial regions.

5. Conclusion

Spectral analysis is a powerful time-series analysis method that is useful to examine particular turbulence regimes and energy cascades within different regions of the global ocean. In this study, we have shown that spectral analysis can be used to identify issues relating to isotropy/anisotropy, intermittency, energy and enstrophy sources and cascades, and identification of turbulence regimes such as three-dimensional, two-dimensional, and geostrophic turbulence regimes. Overall, spectral analysis can be used in coordination with structure functions and observational data to indicate where large-scale circulation models and submesoscale processes must be resolved.

Acknowledgments

NP was supported by a Summer Undergraduate Research Fellowship in Oceanography (SURFO) (National Science Foundation REU grant # OCE-1460819). I would like to thank Dr. Peter Cornillon for his continued guidance and support throughout this process as well as Dr. Baylor Fox-Kemper and Dr. Brodie Pearson for their guidance and contributions to this project.

References

- Callies, J., and R. Ferrari, 2013. Interpreting Energy and Tracer Spectra of Upper-Ocean Turbulence in the Submesoscale Range (1-200 km). *Journal of Physical Oceanography*, **43**, 2456-2474.
- Fox-Kemper, B., B. Pearson, and P. Cornillon. Beyond Spectra: Macroturbulence Observations Select High-Resolution Ocean Models.
- McCaffrey, K., B. Fox-Kemper, and G. Forget, 2015. Estimates of Ocean Macroturbulence: Structure Function and Spectral Slope from Argo Profiling Floats. *Journal of Physical Oceanography*, **45**, 1773-1793.
- Schloesser, F., P. Cornillon, K. Donohue, B. Boussidi, E. Iskin, 2015. *Journal of Atmospheric and Oceanic Technology*, **33**, 1843-1858.
- Tandeo, P., E. Autret, B. Chapron, R. Fablet, and R. Garello, 2013. SST spatial anisotropic covariance from METOP-AVHRR data. *Remote Sensing of Environment*, **141**, 144-148.
- Wang, D.P., C.N. Flagg, K. Donohue, and H.T. Rossby, 2009. Wavenumber Spectrum in the Gulf Stream from Shipboard ADCP Observations and Comparison with Altimetry Measurements. *Journal of Physical Oceanography*, **40**, 840-844.
- Xu, Y., and L.L. Fu, 2011. Global Variability of the Wavenumber Spectrum of Oceanic Mesoscale Turbulence. *Journal of Physical Oceanography*, **41**.

Interactions of euphausiid distributions in the Eastern Tropical North Pacific with the oxygen minimum zone

Shannon L. Riley^{1†}, Dawn M. Outram¹, Danielle M. Moore¹, Thomas Adams², and Karen F. Wishner¹

¹Graduate School of Oceanography, University of Rhode Island, Narragansett, RI, U.S.A.

²Cold Spring Harbor Laboratory, Cold Spring Harbor, NY, U.S.A.

Corresponding author: Shannon Riley (rileysh@oregonstate.edu)

[†]Currently at Oregon State University, Corvallis, OR, U.S.A.

Running head: Riley et al. Euphausiids in OMZs

Key Points:

- Oxygen concentration and temperature affect euphausiid distribution
- Different species have different diel vertical migration patterns
- Small scale depth intervals may have high variability in oxygen concentration and abundance

Key Index Words:

Euphausiids, Oxygen minimum zone, Eastern Tropical Pacific, Distribution, Oxygen concentration, Temperature

Abstract

Euphausiids, commonly called krill, are an important group of zooplankton frequently found in and near oxygen minimum zones (OMZs), midwater depth zones of very low oxygen. Some euphausiid species are adapted to live in or migrate through these zones; others are not. Climate change is predicted to cause vertical and horizontal increases in OMZ size. This may impact euphausiids' ability to live at particular depths or alter their vertical migration patterns. Vertically-stratified and horizontally-sequenced zooplankton samples were collected in the Eastern Tropical North Pacific in early 2017 on the R/V *Sikuliaq* with a MOCNESS net system. Crustaceans, including euphausiids, were removed from the samples, classified into groups and identified to species when possible. Euphausiid abundance and distributional data were analyzed relative to depth, oxygen concentration, and temperature. Comparing day and night vertical tows revealed that, although many euphausiid species spent daylight hours at the same midwater depth, they separated to different depths when migrating towards the surface at night. Horizontal tows at ~430 m showed strong differences in euphausiid abundance associated with changes in oxygen concentration. Habitat diagrams illustrating interactions between temperature, oxygen, and abundance showed that most species had highest daytime abundances in the same temperature water, but were separated by different oxygen concentrations. In fine-scale vertical tows, peak euphausiid abundance occurred during a rapid decline in oxygen concentration over a short depth interval. Because euphausiids are important prey for many animals, changes in their abundance or distribution could impact other populations, including commercially valuable species such as tuna.

(The rest of this section intentionally left blank)

A low-cost Lagrangian float prototype for observations of the biological carbon pump

Jackson Sugar and Melissa Omand

Graduate School of Oceanography, University of Rhode Island, Narragansett, RI 02882

Abstract

A MINature IsOpycNal float [MINION] has been developed to observe sinking particle flux in a Lagrangian frame. The floats are constructed with off-the-shelf parts to minimize cost. Each Wi-Fi enabled Minion is equipped with temperature, pressure and acceleration sensors, real-time clock and a macro lens camera to capture images of marine snow particles as they land on a transparent settling surface. The goal is to be able to resolve episodic variations in carbon flux on time scales from hours to days. Deployments of Minion fleets will allow for sampling over a wide area to improve understanding of the spatial variations of particle size and composition. One of the defining characteristics of the Minion is its reliance on passive buoyancy control which consists of targeting specific isopycnals by varying the density of the float. Optimizing power efficiency will extend endurance of a single deployment while minimizing size. Future Minion iterations will include salinity probes and the ability to adjust photographic light field by sensing ambient light in the euphotic zone. This platform is based on a single expandable Linux computer allowing for continuous and specialized modification for future unforeseen applications.

1. Introduction

Oceanographic dynamics play a pivotal role in global climate cycles. The uptake and sequestering of carbon by the world's oceans exist as a major sink in the global carbon cycle (Schmittner et al. 2008). One of the key interests in carbon cycling is quantifying the production and export of marine particulates from the upper ocean to depth. These marine particles, referred collectively to as marine snow, are comprised of biological materials produced in the upper water column, supported by primary production (Ducklow 2001). Typically a small percentage of surface biomass is fully exported to the deep ocean, where it remains for 1000 to 10,000 years. Therefore, gaining insight into the dynamics of carbon cycling in the oceans is of substantial importance for better interpreting climate regimes. Specifically, quantifying rates of carbon export in time and space is a major topic of interest in oceanographic science.

The challenge faced in quantifying carbon cycling dynamics in the oceans is the necessity for both fine resolution and high volume sampling. Recent developments in technology have made embedded system design cheaper and more accessible, allowing for the collection of novel data sets capable of resolving these phenomena. Motivated by the application of cheap remote sensing technology for in-situ observations of marine snow flux, we initiated development of a Lagrangian imaging platform purpose-built for quantifying rates of marine export.

2. Methods

2.1. Hardware

The main consideration in our design is to allow for low-cost, large-scale construction of many individual MINION platforms for deployment en masse. Thus, design decisions reducing cost and physical footprint while maximizing automated functionality and stability were implemented.

2.1a Physical design

The MINION platform housing all hardware is cylindrical in shape (Fig. 1). The imaging surface occupies one face of the MINION cylinder. The other face of the cylinder is populated by our burn wire assembly and signal LED. This allows for the deployed MINION's center of buoyancy to keep the imaging surface facing upright to properly capture the marine particulates as they accumulate on our platform. Upon completion of a mission, the MINION drops any ballast weight and the center of buoyancy shifts to the imaging surface. When the MINION resurfaces, the signal LED is visible and the onboard GPS transmitter reports its location.

As primarily an imaging platform, the float design is structured around a high resolution cell phone camera mounted to an acrylic imaging surface. Ballast material is mounted opposite the camera, in order to achieve neutral buoyancy for any given target isopycnal. This allows the platform to be deployed as a Lagrangian drifter. The MINION hardware is packed within a semi-compressible rubber material, having properties necessary to withstand undersea pressures. In order to reduce the possibility of leaks, the entire float is designed as a closed system with no external connections.

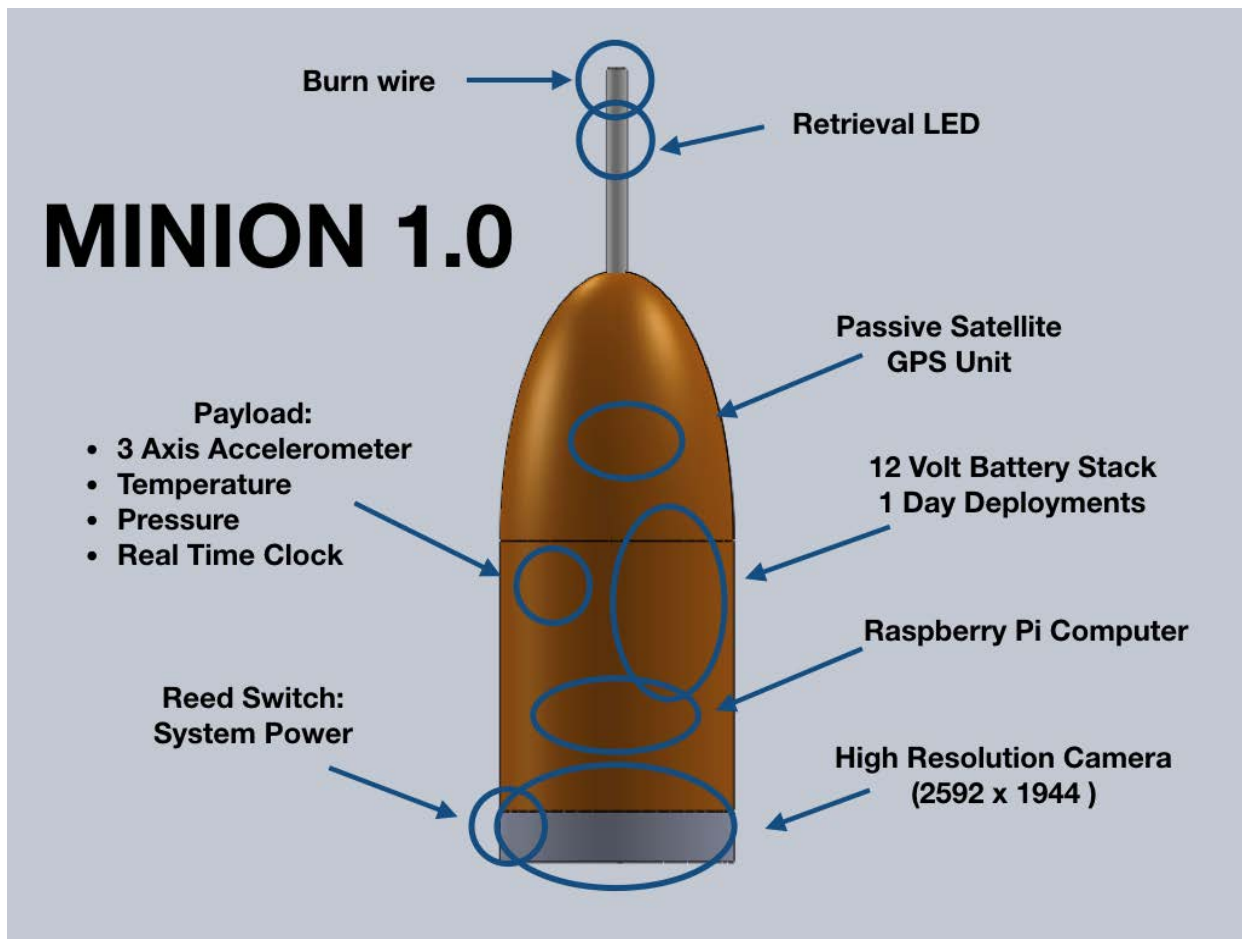


Figure 1: Representation of the first built functional MINION

Due to the enclosed nature of the MINION's electronics, magnetic reed switches are incorporated in order to maintain the battery's charge while in storage. This allows us to shelve these sensors for years before deployments without draining battery.

2.1b Camera and Sensor Payload

With imaging targets for the system being of such small size classes ($> 10 \mu\text{m}$), a camera was needed with sufficient resolution but also a small physical and monetary footprint. The Raspberry Pi foundation camera module V 2.1 was chosen for our application due to the sensor's high resolution (2592 x 1960) and strength in capturing macro images. Captured images of the settling surface are collected at regular intervals over the deployment. Individual images of the settling plate environment over time allow for observations of particle flux to monitor the accumulation of marine particulates (Fig 2).

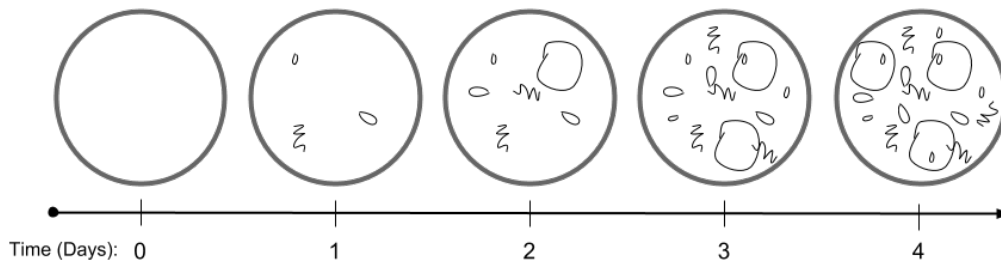


Figure 2: Representation of partial accumulation on imaging surface over deployment

These modules are purpose built for the Raspberry Pi computer and, for their form factor and price, are unparalleled in their performance. Each MINION is equipped with a suite of onboard sensors for measuring temperature, pressure and acceleration data. Recording of temperature and pressure data allows for determination of platform depth and hydrographic characterization water column. The three-axis accelerometer is used to monitor the movement of the MINION to better understand the characteristics of the undersea current.

2.1c) Retrieval Hardware (Burn Wire, LED, GPS)

The autonomous nature of our sensor requires a reliable and repeatable system to terminate a deployment and resurface for recovery. We have opted to incorporate a very simple burn wire assembly consisting of thin, uncoated welding wire as an anode and a $\frac{3}{4}$ inch nut as a cathode. When the system is ready to drop the ballast, a MOSFET switches on and begin conducting electricity across the probes. The anode begins to corrode and eventually weakens to the point of release, allowing for the MINION to float to the surface.

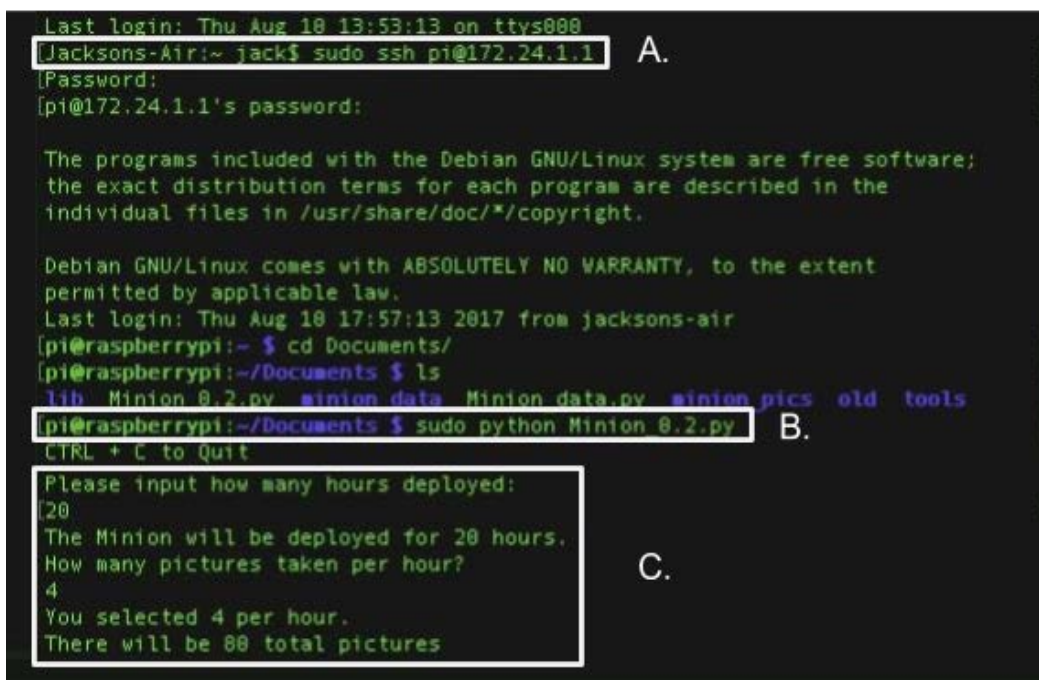
Once the MINION reaches the surface, a signal LED begins to flash at random intervals in order to more easily discern it from any "organic" light source. The on-board GPS unit reports its location to a website, accessible from anywhere.

2.2. SOFTWARE

The MINION's software considerations focus on the importance of simple development, data storage and retrieval of all files generated during deployment. The Linux environment on the Raspberry Pi addresses these concerns. All programs are written in either Python™ or Bash allowing for very simple modifications.

2.2a Remote access: Wi-Fi Access Point/Port Forwarding

One of the challenges of the MINION's physical design is the complete lack of external connections for debugging/communicating with the sensor. The most practical solution to wirelessly communicate with the sensor is over Wi-Fi due to the fast transfer times of the large image files and the ability to log into each sensor individually and make changes to the computer pre-deployment. Each sensor acts as a local router access point allowing any computer or cell phone access to the device through SSH (Fig. 3a), to launch mission scripts (Fig. 3b) and configure mission parameters (Fig. 3c).



```
Last login: Thu Aug 10 13:53:13 on ttys000
[jacksons-air:~ jack$ sudo ssh pi@172.24.1.1] A.
[Password:
[pi@172.24.1.1's password:

The programs included with the Debian GNU/Linux system are free software;
the exact distribution terms for each program are described in the
individual files in /usr/share/doc/*/copyright.

Debian GNU/Linux comes with ABSOLUTELY NO WARRANTY, to the extent
permitted by applicable law.
Last login: Thu Aug 10 17:57:13 2017 from jacksons-air
[pi@raspberrypi:~ $ cd Documents/
[pi@raspberrypi:~/Documents $ ls
lib Minion 0.2.py minion_data Minion_data.py minion pics old tools
[pi@raspberrypi:~/Documents $ sudo python Minion 0.2.py] B.
CTRL + C to Quit

Please input how many hours deployed:
[20
The Minion will be deployed for 20 hours.
How many pictures taken per hour?
[4
You selected 4 per hour.
There will be 80 total pictures] C.
```

Figure 3: Terminal entries for MINION deployment. A) Gain shell access. B) Launch mission scripts. C) Configure missions.

We make use of the software Screen in order to launch multiple terminal instances simultaneously that are not contingent on login status. Simply put, the changes in the scripts pre-deployment are implemented and instances continue running for their full life cycle until recovery.

2.2b Data acquisition, management, and synchronization

The deployment of multiple MINIONS as a collective array mandates a robust global data synchronization. All MINION floats are equipped with a low float real-time clock. This freestanding clock communicates with the Raspberry Pi over i2c and is calibrated to internet time, UTC. Every time a photo is taken or a sensor is read, a timestamp is recorded to better

interpret any data gathered. This is advantageous in order to directly compare other MINIONs samples within the same time scale.

All data acquisition is automated and independent. Software was developed to sample sensor data and saved them locally to a .csv file on the float. All data and photos are timestamped and organized into two folders for efficient data recovery at the completion of the deployment cycle.

2.3 Mission Life Cycle

Data collection via the MINION platform is meant to be as simple and automated as possible. Missions can be broken down into three distinct categories; Deployment, Mission, and Recovery (Fig. 4). The ultimate goal is to be able to easily train scientists (i.e. end users) in MINION-specific sensor configuration and deployment. This section illustrates the stepwise process of MINION deployment.

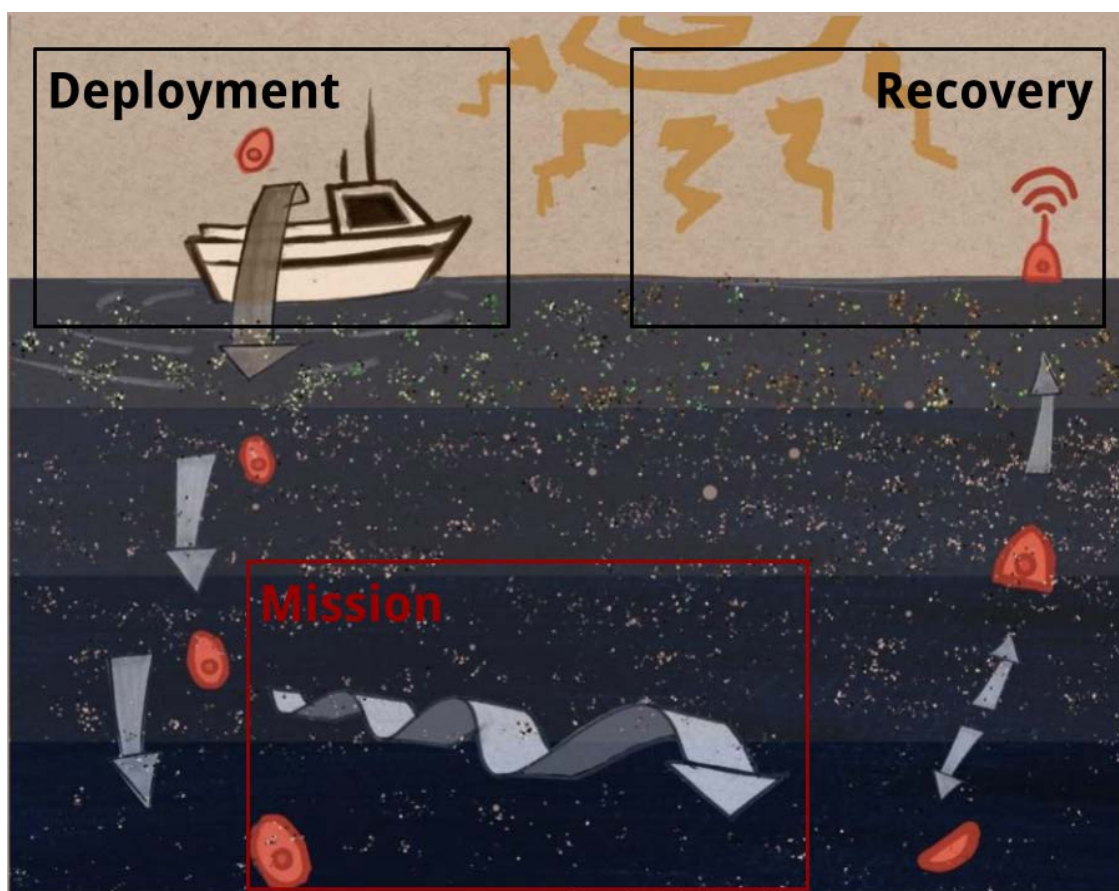


Figure 4: Heuristic representation of typical MINION mission cycle

Deployment

Step one: Calculate and attach ballast to burn wire so the MINION is neutrally buoyant at the chosen isopycnal.

Step two: Log into the MINION and define the mission. The scripts prompt the user for deployment length and sample rates.

Step three: Deactivate Wi-Fi and drop off in open ocean.

Mission

Once deployed, the MINION settles on the target isopycnal and continuously sample data as configured. At mission completion, the burn wire fires and separates the ballast from the MINION allowing it to resurface.

Recovery

Step four: Once MINION resurfaces, the scientist receives a notification from SzPOT Trace[®] website along with GPS feed of the float updated in real time.

Step five: Activate i-Fi. Log into MINION and retrieve folders ~/Documents/minion_pics/* and ~/Documents/minion_data/* using Secure Copy Protocol.

3. Discussion

An iterative design process was required for completion of this ambitious design project, resulting in the completion of a functional prototype platform as well as the initial rendering of an updated platform design. MINION 1.0 was designed and constructed in less than 4 weeks. The platform as a whole is still in its infancy, and continued modification and optimization are necessary to ensure a robust and reliable system.

3.1 Current standing

Recently we have shifted our focus to miniaturizing our electronics footprint while minimizing battery consumption. We are also developing printed circuit boards in the same form

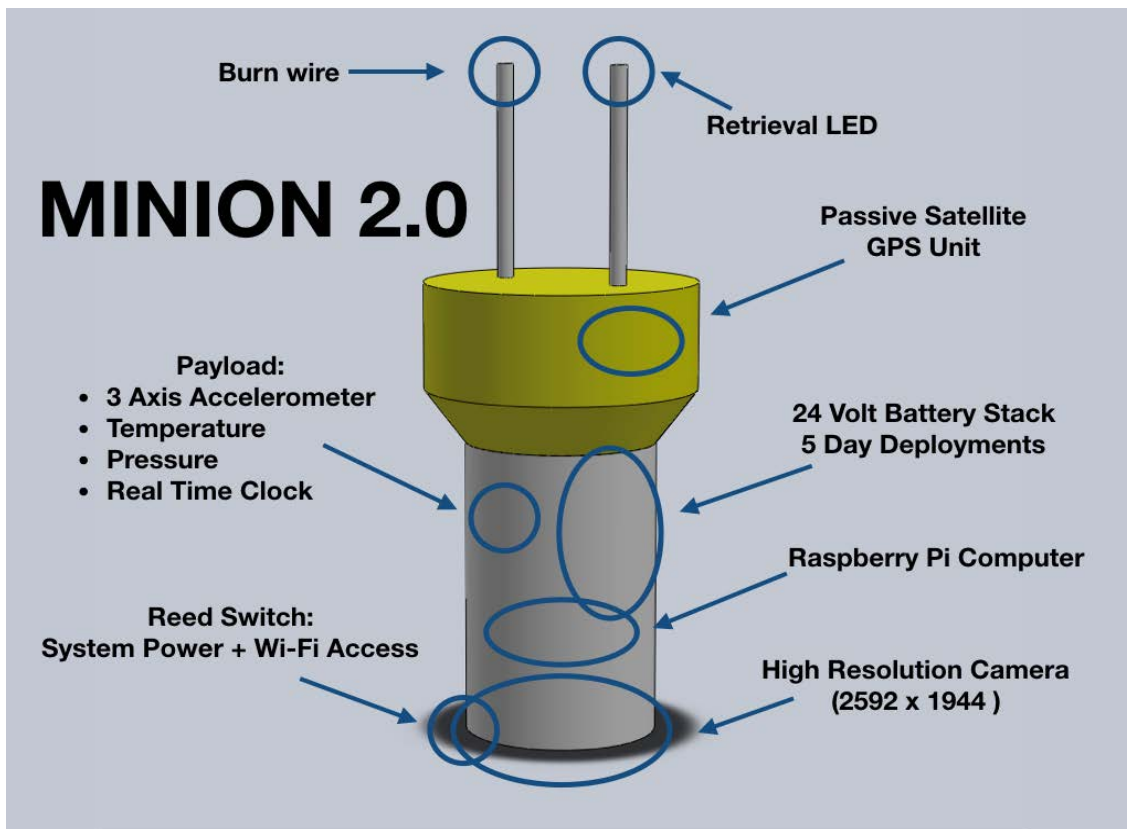


Figure 5: Hardware schematic of MINION 2.0 redesign

factor as the Raspberry Pi computer with the goal of reducing all onboard electronics to a single PCB “hat”. This will not only reduce fabrication time but also increase quality control by reducing the possibility of hardware failure.

These changes, and others, are reflected in MINION 2.0 (Fig. 5). The retrieval LED and burn wire have been separated to simplify production. Additionally, the body of the MINION has been reshaped to aid in flotation given that the previous MINION design would not orient upright for retrieval, harming GPS signal integrity and signal LED visibility. The power system has been reworked to greatly increase life span of the sensor to roughly 5x times that of MINION 1.0. One of the main contributors to achieving this goal was the incorporation of a Wi-Fi access reed switch which allows us to toggle the access point on and off, saving almost ~0.2 Watts, a third of our power draw. These changes to the MINION platform together increase the reliability and functionality of the float.

3.2 Future Development

In the future, we plan to incorporate fish chip hydrophones (Recksiek et al. 2006). These devices, the size of a small lipstick, will allow to more closely track the movements of the MINIONS underwater during their 5-day maximum deployment. The incorporation of fish chip technology with the MINION platform is simple in that the sensor is mounted to the exterior of the MINION and does not require any interfacing with onboard electronics of the float. The fish chip listens for pings every hour for 5 minutes. While the MINIONS are deployed, the chips are pinged by a sound source located on the boat during the intervals at which the fish chip is actively recording. Upon retrieval, the arrival times of the pings on the fish chip allow us to monitor the movements of each individual MINION. Without these data, the MINION trajectory could only be characterized by its deployment and retrieval locations. With the addition of the fish chip functionality, the MINION becomes localized over its deployment as do the collected data.

4. Conclusion

We have designed a low cost, automated Lagrangian profiler capable of collecting *in situ* image data. This platform will provide a means of quantifying rates of carbon export through simple image processing procedures. We anticipate gathering real world data from the first open water trials imaging marine particulates in the near future. Our current interests are focused on quantifying particle dynamics; however, this platform will be flexible in application as the MINION continues to evolve.

Acknowledgments

JS was supported by a Summer Undergraduate Research Fellowship in Oceanography (SURFO) (National Science Foundation REU grant # OCE-1460819).

References

- Ducklow, H. W., Steinberg, D. K., & Buesseler, K. O. (2001). Upper ocean carbon export and the biological pump. *OCEANOGRAPHY-WASHINGTON DC-OCEANOGRAPHY SOCIETY-*, 14(4), 50-58.
- Recksiek, C. W., G. Fischer, H. T. Rossby, S. X. Cadrin, and P. Kasturi (2006). Development and Application of ‘RAFOS Fish Tags’ for Studying Fish Movement. *ICES CM 2006/Q:16*.

Schmittner, A., Oeschies, A., Matthews, H. D., & Galbraith, E. D. (2008). Future changes in climate, ocean circulation, ecosystems, and biogeochemical cycling simulated for a business-as-usual CO₂ emission scenario until year 4000 AD. *Global Biogeochemical Cycles*, 22(1).

Optics and Phytoplankton in Narragansett Bay, RI**Kyle J. Turner¹, Audrey Ciochetto² and Colleen Mouw²**¹Department of Earth Science, George Mason University, Fairfax, VA²Graduate School of Oceanography, University of Rhode Island, Narragansett, RI**Abstract**

Deriving accurate and useful information from satellite spectral measurements of optically-complex coastal waters remains a challenging research question. Optical properties and phytoplankton variability of Narragansett Bay are examined using existing data sources, *in situ* sampling, laboratory analysis, and historic satellite imagery. Surface seawater samples are collected daily at the University of Rhode Island's Graduate School of Oceanography (GSO) dock, and surface and bottom samples are collected weekly at Narragansett Bay Station 2, the regular sampling site of GSO's long-term plankton survey (LTPS). Samples are processed for particulate absorption, chlorophyll a (Chl-a), and colored dissolved organic matter (CDOM). High-resolution images of individual phytoplankton cells are obtained with an Imaging FlowCytobot (IFCB). Phytoplankton variability and abundance from IFCB and LTPS measurements are compared. Medium Resolution Imaging Spectrometer (MERIS) full resolution (300m) imagery of Narragansett Bay and the surrounding region is obtained and processed with three atmospheric correction methods, and compared to *in situ* radiometric measurements from the Aerosol Robotic Network - Ocean Color (AERONET-OC) site at Martha's Vineyard Coastal Observatory (MVCO). MERIS remote-sensing reflectance (R_{rs}) values for Narragansett Bay Station 2 seem to show responses to LTPS Chl-a concentration, however, other constituents, such as non-algal particles, seem to have a strong influence on the reflectance signal. These investments will help to improve understanding on the influence of different optically significant constituents in Narragansett Bay on the spectral signal measured by satellites, and help facilitate continued optical and imaging observations in the bay using a full suite of *in situ* optical instrumentation.

Proposal to the National Science Foundation Graduate Research Fellowship Program**Shelf-water influx: Optical and phytoplankton community responses
in Narragansett Bay, Rhode Island**

(The rest of this section intentionally left blank)

A Search for Earthquakes in Iran Using Remote Sensing Data

Melanie Wallace, Sam Bell, Meng Wei

Graduate School of Oceanography, University of Rhode Island, Narragansett, RI 02882
Corresponding author: matt-wei@uri.edu

Abstract

It is challenging to determine the accurate location and focal mechanism of earthquakes in areas with poor coverage of local seismic stations. Remote sensing data, specifically, the interferometric synthetic aperture radar (InSAR), have proven a useful tool for locating earthquakes that cause surface deformation. This technology is most useful for events that are shallow (less than twenty kilometers) and large (with a magnitude greater than 5 on the Richter scale). For this research, we used InSAR data from Sentinel-1A to search for earthquakes in Iran between January 2013 and August 2017. Out of the nine earthquakes with interferogram coverage, we found a magnitude 6.1 earthquake at 35.7824°N 60.39°E that caused a displacement over 1 cm. The best fit model suggests that this event occurred 4.766 km below the earth's surface with a strike of 219 °, a dip of 50 °, and a rake of 135 °. This event, along with other events identified earlier by InSAR, can be used as references to relocate other events. Together, this will improve the earthquake locations in Iran, which are critical in seismic monitoring of nuclear tests.

1. Introduction

Finding seismic activity in Iran using remote sensing data and accurately locating the epicenter of those events can create reliable reference points. Those reference points are necessary for knowing the location and movement of fault lines, identifying nuclear testing sites, and the accurate location of other seismic events. In Iran, the Arabian plate is subducting beneath the Eurasian plate. They collide within Iran, putting the entire country in a collision state, resulting in frequent earthquakes.

The standard way to locate earthquakes is to use at least three seismic monitoring devices, which record the time of seismic waves passing the seismic stations. The location is then triangulated from the times when the waves reached each device. However, Iran has few local seismic stations, and because the margin of error increases significantly with distance, the location error

determined by remote seismic stations can be as large as tens of km.

Another way to locate events is by using interferometric synthetic aperture radar (InSAR) to find the surface displacement in terrain caused by earthquakes. The advantage is high accuracy, usually within a few km. However, it is not always possible to see events in this way; the ground displacement must be significant and there must be two radar images, one before and one after the event. As a result, the number of events identified by remote sensing data is low at about 2 events per year. A previous study from 2013 looked for seismic activity in Iran, also using remote sensing data. Over the course of ten years, 17 events were found (Barnhart, 2013).

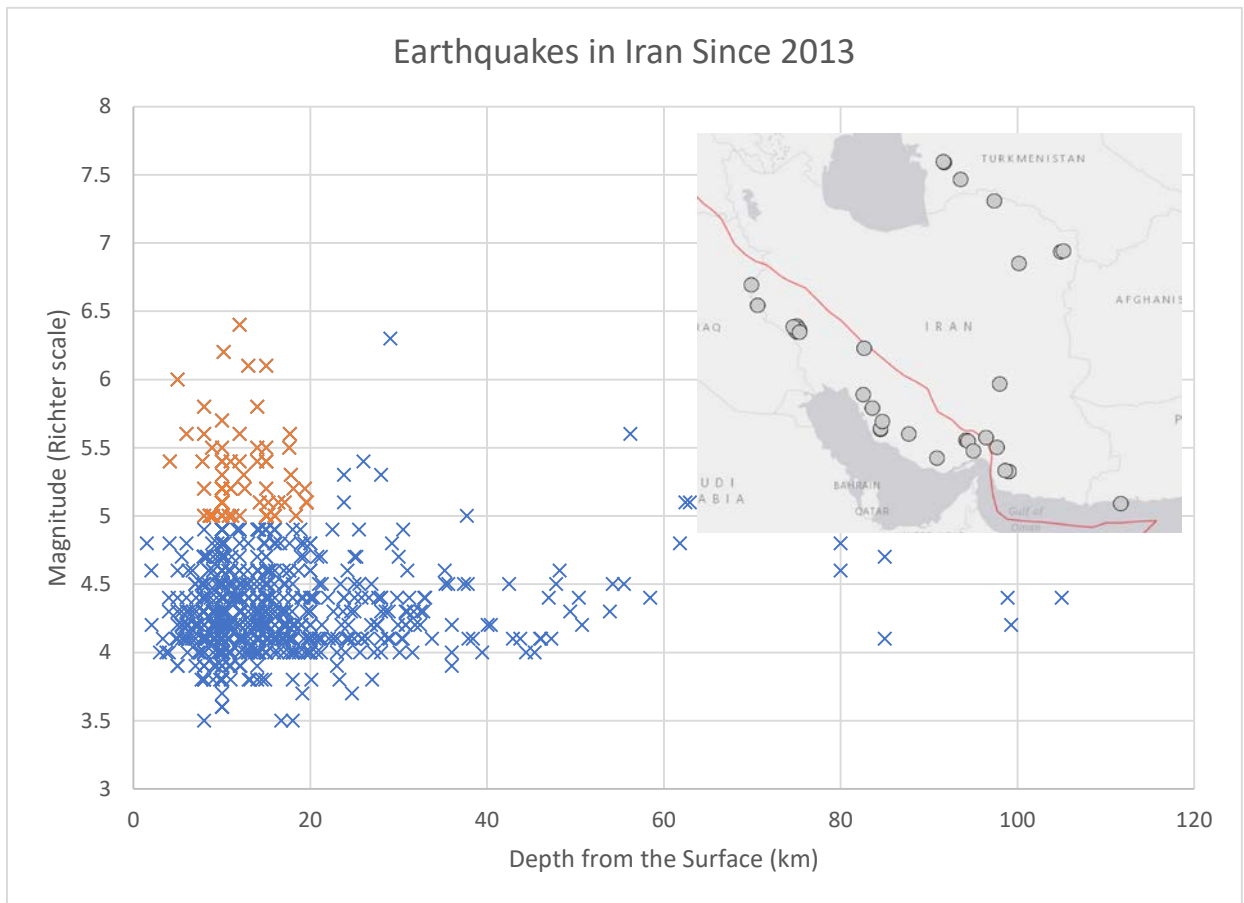


Figure 1. All earthquakes in Iran since January 1st 2013 (total 109) from the USGS earthquake catalog, with depth from surface in km and magnitude on the Richter scale. Earthquakes below 20 km and above 5 in magnitude are more likely to be seen using remote sensing (orange), and their locations are shown on map of Iran. What is the red line on the insert?

A comprehensive approach is to combine both remote sensing and seismic data. Using remote sensing identified events as references to relocate other events nearby that were found using the seismic approach. In this project, we searched nine earthquakes using satellite Sentinel-1A.

2. Methodology

2.1 InSAR processing

We used InSAR images (interferometric synthetic aperture radar) to locate earthquakes. InSAR is a microwave imaging system with cloud-penetrating capabilities. Each SAR image is composed of

individual pixels which have amplitude and phase information. The amplitude depends on the roughness of the terrain, slope, and dielectric constant. Typically, exposed rocks and urban areas show strong amplitudes, whereas smooth flat surfaces like a calm lake show low amplitudes. Taking the interferogram of the phase information from two SAR images, generates a Digital Elevation Model as well deformations in the terrain (Ferretti, 2007). Because the antenna footprint moves at the satellite speed along its orbit, the capability of imaging a strip is 445 km long every minute. For this project, we have been using data from the Sentinel 1A which came online in 2013.

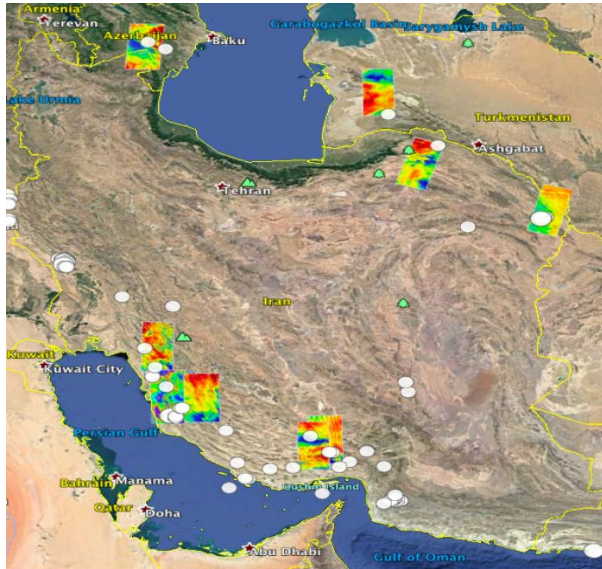


Figure 2. Processed interferograms, with a total of 9 earthquakes examined.

A list from the United States geological survey was compiled of all the earthquakes in Iran since January 1st, 2013 (Figure 1). These data were found using remote seismic stations, which can have location errors as high as tens of km. An earthquake must be at least a 5 on the Richter scale to cause that kind of surface displacement, as well as be fairly close to the surface. It is also difficult to look for earthquakes that happen in clusters. If an earthquake has large aftershocks that occur very close to the original event, the surface displacement cannot always be tracked back to which earthquake caused it.

Sentinel-1A data from January 2013 to August 2017 were then downloaded from the European -Space Agency. The data were

processed using the open source software GMTSAR (Sandwell et al. 2011). A 90-m resolution Shuttle Radar Topography Mission (SRTM) digital elevation map (DEM) was used to remove the topographic signal (USGS2004). A Gaussian filter with a wavelength of 200 m was used to filter the phase image and software SNAPHU (Chen & Zebker 2002) was used to unwrap it, both were built-in in GMTSAR.

2.2 Grid search for best source parameters

Once an event is found, parameters of interest are calculated. Type of fault, strike, dip, rake, length, width, and moment tensor are particularly important. The parameters are found by using forward modeling to create a model of the surface displacement based on Okada (1985), with the intent to get the model as close as possible to the surface displacement seen in the interferograms. For simplicity, we assume a uniform slip and a pure double couple moment tensor. Once the model is reasonably close to the real data, a grid search is performed to find the best fitting model.

2.3 Using topography to reduce atmospheric noise

Atmospheric noise is the largest source of error in InSAR, which can be reduced by topography correction (Bekaert, 2015). Assuming the atmosphere noise is linearly related to the topography, the interferometric tropospheric phase $\Delta\psi_{\text{tropo}}$ can

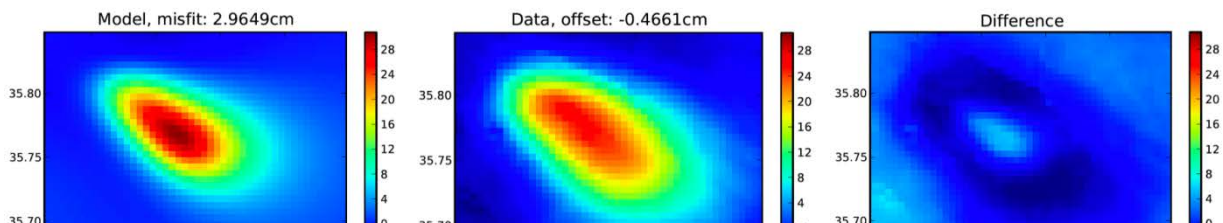


Figure 3. Results of the grid search for April 4th, 2017 event. Computed model (left), actual data (middle), difference between the two (right).

be estimated from the relationship between the interferometric phase and the topography:

$$\Delta\phi_{\text{topo}} = K_{\Delta\phi}h + \Delta\phi_0,$$

where K is a scale factor, h is the topography, and $\Delta\phi_0$ is a constant.

3. Results

3.1 InSAR search

Thirty interferograms (wrapped and unwrapped) were processed and examined (figure 2). On three separate occasions, multiple images were produced covering the same area. This was done when the first image had too much atmospheric noise for an event to be observed. Events are found by looking for either rapid phase change (wrapped interferograms) or rapid displacement (unwrapped interferograms) near the USGS determined locations. The interferogram produced for the April 4th 2017 event is a very obvious event. It was

produced from two images taken on March 25th and April 6th, 2017. Another possible event was observed in southern Iran, the earthquake occurred on January 1st, 2015. A rapid phase change was observed in one interferogram (10/27/14 – 5/7/15) but not another (12/30/14 – 2/16/15), suggesting the suspected signal in the first interferogram is atmospheric noise.

3.2 Source parameter modeling

One event was found in north western Iran. It had a magnitude of 6.1 and occurred on April 4th of this year according to USGS. There were two aftershocks, one on the same day and one occurring about one month later (May 5th), both of magnitude 5.1. The event had an average surface displacement of 3.5 cm, and was an oblique slip fault. The event occurred ~4.8 km below the earth's surface with a strike of 219°, a dip of 50°, and a rake of 135°. The epicenter of the event occurred at 35.7824 °N 60.39°E. Remote seismic stations had the epicenter located at 35.7971°N 60.4318°E, which is approximately 4 km away from the center of the fault displacement.

3.3 Topographic correction

The topography corrected linear approach can be seen in figure 5, as demonstrated on the found event. The standard deviation of the original unwrapped interferogram is 17.35, whereas the corrected interferogram standard deviation is significantly

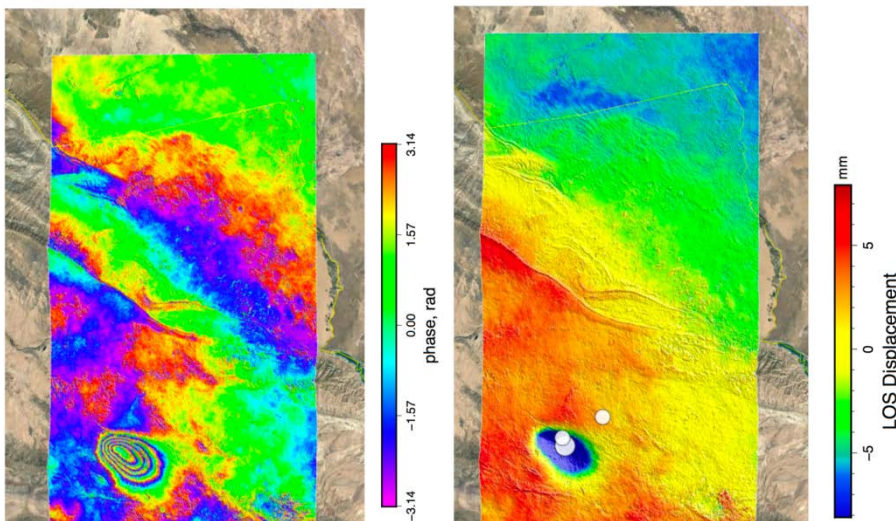


Figure 4. Wrapped interferogram (left) in phase (radians), unwrapped interferogram (right) in millimeters. Interferograms processed from images taken on March 25th and April 6th. Path 20, frame 473, swath 3. In the right figure, negative phase indicates a decrease in line of sight (LOS) distance. The white circles in the right figure are the USGS determined locations of the main shock (M6.1 4/5/17) and two large aftershocks (M5.1 4/5/17, M5.1 5/2/17).

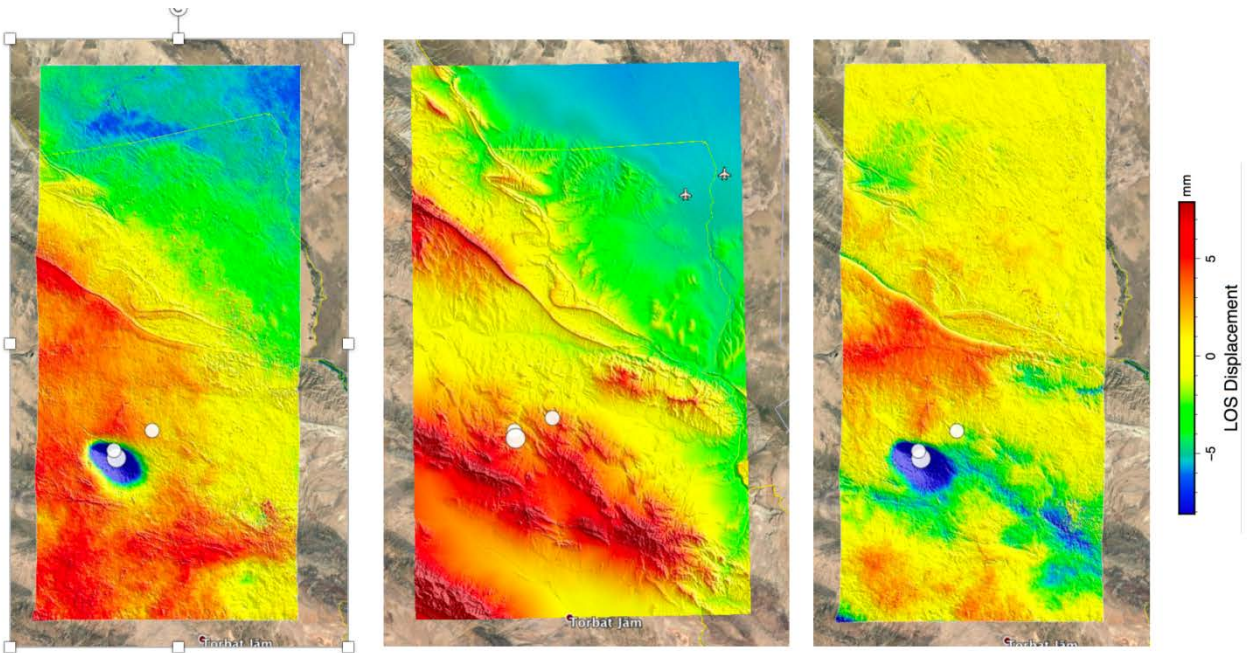


Figure 5. Line of sight (LOS) map (left), Topographic generated model (middle), Topographic Corrected Interferogram (right). The corrected interferogram was calculated by taking the difference between the LOS and the topographic model, then multiplying by scale (0.0106).

less at 2.82. There is also a decrease in means, with the original interferogram having a mean of 0.97 mm and the corrected one with a mean of -0.20.

4. Discussion

Usable interferograms are difficult to compile for several reasons: satellites shift course, the pair of images must have matching orbits (ascending versus descending) and polarization, and there are time blocks when satellites are offline and no images are taken. The challenge that we encountered most during this project was atmospheric noise. Atmospheric noise occurs because the two images are not taken at the same time and difference in atmospheric conditions (different atmospheric humidity, temperature, and pressure) can affect the radiation travel path (Ferretti, 2007). It is possible to quantitatively describe this turbulence as the covariance in the interferometric data (Hanssen, 2011).

There was another image processed for the April 4th event (process from images taken on March 25th and April 18th of 217), unfortunately there was so much atmospheric noise that the data were rendered unusable. Another interferogram was processed, using different initial images, and the April 4th event was identified.

5. Conclusion

We have processed 30 interferograms from Sentinel-1A satellite covering 9 earthquakes between January 1st, 2013 – July 30th 2017. We found a Magnitude 6.1 event on April 4th, 2017 with displacement about 3.5 cm LOS. We modeled the displacement with a half-space elastic model. We found the best fitting image through a grid search. The best-fit model suggested that this earthquake occurred ~4.8 km below the earth's surface with a strike of 219°, a dip of 50°, and a rake of 135°. The event found in northwestern Iran was 4 km away from where the seismic monitoring devices placed it.

With this one event, the location accuracy can be improved by using it as a reference to relocate other events in northwestern Iran that were found using the seismic approach.

6. Acknowledgments

M. Wallace was supported by a Summer Undergraduate Research Fellowship in Oceanography (SURFO) (National Science Foundation REU grant # OCE-1460819).

7. References

- Barnhart, W. D., Lohman, R. B., & Mellors, R. J. (2013). Active accommodation of plate convergence in Southern Iran: Earthquake locations, triggered aseismic slip, and regional strain rates. *Journal of Geophysical Research: Solid Earth*, 118(10), 5699-5711. doi:10.1002/jgrb.50380
- Bekaert, D., Walters, R., Wright, T., Hooper, A., & Parker, D. (2015). Statistical comparison of InSAR tropospheric correction techniques. *Remote Sensing of Environment*, 170, 40-47. doi:10.1016/j.rse.2015.08.035
- Chen, C.W. & Zebker, H.A., 2002. Phase unwrapping for large SAR interferograms: statistical segmentation and generalized network models, *IEEE Trans. Geosci. Remote Sens.*, 40, 1709–1719.
- Ferretti, A. (2007). InSAR principles: guidelines for SAR interferometry processing and interpretation. Noordwijk: ESA.
- Hanssen, R. F. (2011). Radar interferometry: data interpretation and error analysis. Dordrecht: Springer.
- Sandwell, D., Mellors, R., Tong, X., Wei, M. & Wessel, P., 2011. Open radar interferometry software for mapping surface deformation, *EOS, Trans. Am. geophys. Un.*, 92(28), 234, doi:10.1029/2011EO280002.
- USGS (United States Geological Survey), 2004. Shuttle Radar Topography Mission, 1 Arc Second Scene SRTM u03 n008e004, Unfilled Unfinished 2.0, Global Land Cover Facility, University of Maryland, College Park, Maryland.
- USGS Earthquake Hazards Program. (n.d.). Retrieved August 08, 2017, from <https://earthquake.usgs.gov/>
- Vertex: ASF's Data Portal. (n.d.). Retrieved August 08, 2017, from <https://vertex.daac.asf.alaska.edu>